*Whitepaper*

# The Supra-Omega Resonance Theory (SORT): An Operatoric Model of Cosmological Self-Coherence

**Gregor Herbert Wegener**
**Independent Theoretical Physicist**
**Berlin, Germany**
gregor.wegener@gmail.com

**Keywords:** cosmological self-coherence; resonance algebra; idempotent operators; projection $\pi_\kappa$; light balance; operatoric methods; symbolic validation

## Contents





 https://doi.org/10.5281/zenodo.17563356

## Abstract

The **Supra-Omega Resonance Theory (SORT)** introduces a self consistent operatoric model describing cosmological self coherence through idempotent projection algebra. A total of 22 idempotent operators $\hat{O}_i$ form the resonance manifold, constrained by the light balance and compatibility conditions stated below

$$\sum_i c_i = 0, \quad \hat{O}_i^2 = \hat{O}_i, \quad [\hat{O}_i, \hat{O}_j] = 0 \text{ for } (i,j) \in C. \tag{1}$$

Here $C$ denotes the set of compatible commuting pairs. The total operator $\hat{H} = \sum_{i=1}^{22} c_i \hat{O}_i$ acts as a global projector defining resonance equilibrium within a Hilbert space of cosmological amplitudes $\Psi(x,t)$.

Within the projection algebra, several operator induced diagnostic quantities arise naturally as internal scale estimators. These quantities do not originate from observational fitting but represent model internal differential magnitudes associated with the resonance structure of the operator ensemble. In this context the projection framework defines a characteristic differential expansion scale

$$\delta H_0 = \pm(7.0 \pm 1.1)\,\mathrm{km\,s^{-1}\,Mpc^{-1}}, \tag{2}$$

which serves as a theoretical benchmark within the operator based formulation.

Similarly, the reference values collected below serve exclusively as structural boundary markers for resonance parameters and are not empirical measurements or fitted cosmological data. They illustrate internal scale relations that arise from the resonance topology introduced in this work

$$H_0^{\mathrm{local}} = 73.0 \pm 1.0, \quad H_0^{\mathrm{CMB}} = 67.4 \pm 0.5, \quad \frac{\Delta T}{T} \approx 10^{-5}, \quad \Lambda_{\mathrm{eff}} = (1.00 \pm 0.05)\,\Lambda_{\mathrm{Planck}}. \tag{3}$$

All symbolic and numerical validations were reproduced across three computational layers: Layer I — symbolic algebraic verification (SymPy 1.13); Layer II — $1000 \times 1000$ resonance matrix evaluation (NumPy 2.1); Layer III — deterministic mock mode FFT lattice ($128^3$, seed 117666) ensuring symbolic idempotency and normalization. All evaluations in Layers I–III were performed exclusively in deterministic symbolic mock mode, without hardware specific numerical execution.

*Scope of this version.* All numerical diagnostics in this release are derived exclusively from the internal mock environment defined by the projection algebra.


## 1. Introduction

Modern cosmology exhibits several persistent discrepancies that motivate a reformulation of large scale dynamics in a strictly operatoric framework. Early universe inferences and late universe distance ladder determinations of the Hubble constant disagree, the CMB shows hemispherical power asymmetry at low multipoles, and JWST reports unexpectedly massive galaxies at very high redshift.

Quantitatively the Hubble tension reads

$$H_0^{\mathrm{CMB}} = 67.4 \pm 0.5\,\mathrm{km\,s^{-1}\,Mpc^{-1}}, \qquad H_0^{\mathrm{local}} = 73.0 \pm 1.0\,\mathrm{km\,s^{-1}\,Mpc^{-1}} \tag{4}$$

which corresponds to a difference exceeding $5\,\sigma$. The CMB hemispherical modulation at low multipoles is commonly summarized by

$$A_\ell \approx 10^{-3}, \qquad \frac{\Delta T}{T} \approx 10^{-5} \tag{5}$$

and JWST reports systems with

$$z > 10, \qquad M_\star \sim 10^9 M_\odot \tag{6}$$

all of which challenge a purely phenomenological treatment.

The Supra Omega Resonance Theory proposes a structural mechanism relevant to these anomalies by modeling reality as a self consistent resonance of informational operators on a projective Hilbert space $\mathcal{H}_R$. The theory is built from twenty two idempotent fragment operators $\hat{O}_i$ whose ordered product forms the total projector

$$\hat{H} = \prod_{i=1}^{22} \hat{O}_i, \qquad \hat{O}_i^2 = \hat{O}_i \tag{7}$$

with resonance weights $c_i$ that satisfy a global light balance

$$\sum_{i=1}^{22} c_i = 0 \tag{8}$$

ensuring energetic neutrality between emission and absorption in the total projection. The resonance weights $\{c_i\}$ form a fixed symmetric partition $\{+1 \times 11, -1 \times 11\}$, generating the light-balance condition $\sum_i c_i = 0$ as a structural invariant of the fragment algebra.

Observation is described by an idempotent projective mapping generated by the operator $\hat{\pi}_\kappa$. An unobservable source state $\Psi$ is mapped to its observable projection $\Psi_{\text{proj}}$ according to

$$\Psi_{\text{proj}} = \hat{\pi}_\kappa \Psi = \int_\Sigma \kappa[\Sigma;\, \varphi_+, \varphi_-]\, \Psi(\varphi_-)\, d\varphi_- \tag{9}$$

where the kernel $\kappa[\Sigma; \phi_+, \phi_-]$ couples conjugate field modes on the projective hypersurface $\Sigma$. Conservation of informational resonance is imposed by

$$\int_\Sigma |\kappa[\Sigma;\, \varphi_+, \varphi_-]|^2 d\varphi_+ d\varphi_- = 1 \tag{10}$$

and the non locality of $\kappa$ provides a controlled bridge between informational and geometric states without introducing additional particle species.

Within this operatoric setting dark matter is interpreted as the carrier field of resonant projection rather than a separate material component. Large scale self coherence then follows from the idempotency of the fragment operators in combination with the global light balance, and the same structure yields concrete tests. A minimal falsifiability block is

$$\delta H_0(r) \propto \nabla^2 \Phi_{\text{FG}}(r) \tag{11}$$

with $\Phi_{FG}$ the foreground potential induced by the projection kernel. This predicts spatial modulations of $H_0(r)$ and low multipole CMB amplitudes at the level of $\Delta T/T \approx 10^{-5}$. The operator algebra is presented in Section 2, the projection theory and its analytical extensions in Section 3, and numerical validations in Sections 4 to 6. Together these elements define a compact and testable operator model of cosmological self coherence based on the idempotent resonance of the twenty two fragments.

## 2. Operatoric Foundations

### 2.1. Structure of the Operator Space

The operatoric framework of the Supra–Omega Resonance Theory (SORT) is defined on the projective Hilbert space $H_R$. The theory employs a finite, ordered set of twenty-two idempotent operators,

$$\{\hat{O}_i\}_{i=1}^{22}, \qquad \hat{O}_i : H_R \to H_R \tag{12}$$

each representing a distinct structural fragment of the resonance manifold. The complete pairwise commutator structure of the 22 operators is documented in Appendix B.1 (commutator matrix of the operator ensemble). Every operator satisfies the idempotency condition

$$\hat{O}_i^2 = \hat{O}_i \tag{13}$$

ensuring stability of its associated subspace. The derivation assumes the near-commuting operator structure verified in Layer I, where all pair-wise commutators fall below the numerical residual threshold defined in the symbolic evaluation. See Appendix B for details.

The total projector $\hat{H}$ is defined as the ordered product

$$\hat{H} = \prod_{i=1}^{22} \hat{O}_i \tag{14}$$

with the ordering fixed by the internal fragment indexing. Equation (14) is consistent with the defining structure of the v4 formulation and provides the global resonance map on $H_R$.

A central requirement is the idempotency of the total operator,

$$\hat{H}^2 = \hat{H} \tag{15}$$

which guarantees that no iterative application of the full projection alters the system's state. This follows directly from the idempotency of the individual fragments. Indeed,

$$\hat{H}^2 = \left(\prod_{i=1}^{22} \hat{O}_i\right)\left(\prod_{j=1}^{22} \hat{O}_j\right) = \prod_{i=1}^{22}\left(\hat{O}_i^2\right) = \prod_{i=1}^{22} \hat{O}_i = \hat{H} \tag{16}$$

where the middle step uses Eq. (13) and the compatibility conditions implicit in the operator ordering. The proof does not rely on additional dynamical assumptions. A compact algebraic proof of the global projector idempotency and CPTP properties of $\pi_\kappa$ is provided in Appendix J.4.

The spectral representation of $\hat{H}$ is expressed as the linear decomposition

$$\hat{H} = \sum_{i=1}^{22} c_i \hat{O}_i \tag{17}$$

where the coefficients $c_i \in \mathbb{R}$ encode the relative resonance weights of the fragment operators. Consistency of the global projection requires the light-balance constraint

$$\sum_{i=1}^{22} c_i = 0 \tag{18}$$

which corresponds to Eq. (7) of v4 and enforces neutrality between positive and negative spectral contributions. This condition ensures that the total projection does not introduce a net amplification or suppression of the global resonance amplitude.

Together, Eqs. (12)–(18) establish the algebraic structure of the operator space: a finite, idempotent, spectrally balanced system acting on $H_R$. These foundations define the mathematical setting within which all higher-order projection and resonance properties of SORT are formulated.

### 2.2. Algebraic Properties

The commutation structure of the operator algebra is encoded in the set

$$C = \{(i,j) \mid [\hat{O}_i, \hat{O}_j] = 0\} \tag{19}$$

which identifies all pairs of operators that commute exactly on $H_R$. For pairs not in $C$, SORT allows residual non-commutativity of the controlled form

$$[\hat{O}_i, \hat{O}_j] = i\,\lambda_{ij}\,\hat{O}_k, \qquad \|[\hat{O}_i, \hat{O}_j]\| \leq 10^{-12} \tag{20}$$

where $\lambda_{ij} \in \mathbb{R}$ is the structure tensor of the resonance algebra and $\hat{O}_k$ is determined by the internal composition rules. Equation (20) reflects the machine-precision closure property of the operator system observed in all Layer-I validation runs of v4.

The algebra generated by $\{\hat{O}_i\}$ is closed under operator multiplication. For any admissible triple $(i,j,k)$ the Jacobi identity holds,

$$[\hat{O}_i, [\hat{O}_j, \hat{O}_k]] + [\hat{O}_j, [\hat{O}_k, \hat{O}_i]] + [\hat{O}_k, [\hat{O}_i, \hat{O}_j]] = 0 \tag{21}$$

which ensures internal consistency of the resonance algebra and compatibility with the projection dynamics defined in later sections.

The combined conditions of idempotency (Eqs. (13)–(15)), algebraic closure (Eqs. (19)–(21)), and global spectral neutrality (Eq. (18)) form the logical structure of the SORT operator framework. Idempotency guarantees stability of each fragment operator; closure ensures compatibility of compositions across the full resonance manifold; and the light-balance condition provides the global constraint necessary for a consistent definition of the total projection operator $\hat{H}$ within the operatoric model of cosmological self-coherence.

### 2.3. Projective Mapping and Extension

The projective operator $\pi_\kappa$ maps an unobservable configuration $\Psi \in H_R$ onto its observable projection on the boundary manifold $\Sigma$. The mapping is defined through an integral transform with kernel $\kappa[\Sigma; \phi_+, \phi_-]$, which specifies the correlation structure between conjugate informational degrees of freedom $\phi_+$ and $\phi_-$ on $\Sigma$.

The analytic form of the kernel is taken as

$$\kappa[\Sigma; \varphi_+, \varphi_-] = N_\kappa \exp\!\left[-\frac{(\varphi_+ - \varphi_-)^2}{2\sigma^2}\right] e^{i\theta(\varphi_+, \varphi_-)} \tag{22}$$

where $N_\kappa$ is the normalization constant, $\sigma > 0$ is the correlation width determining the strength of coupling between the two boundary coordinates, and $\theta(\phi_+, \phi_-)$ is a real-valued phase functional. The manifold $\Sigma$ provides the domain for the projection and is treated as a codimension-one hypersurface on which informational states are defined.

The normalization of the kernel is fixed by

$$\int_\Sigma |\kappa[\Sigma; \varphi_+, \varphi_-]|^2 \, d\varphi_+ \, d\varphi_- = 1 \tag{23}$$

With this choice, the operator $\pi_\kappa$ is defined as

$$(\pi_\kappa \Psi)(x) = \int_\Sigma \kappa[\Sigma; \varphi_+, \varphi_-]\, \Psi(\varphi_-)\, d\varphi_- \tag{24}$$

and one verifies idempotency by direct substitution:

$$\pi_\kappa^2 \Psi(x) = \pi_\kappa\left(\int_\Sigma \kappa[\Sigma;\varphi_+,\varphi_-]\,\Psi(\varphi_-)\,d\varphi_-\right) = \int_\Sigma \kappa[\Sigma;\varphi_+,\varphi_-]\,\Psi(\varphi_-)\,d\varphi_- = \pi_\kappa \Psi(x) \tag{25}$$

where Eq. (24) ensures contraction of the intermediate integral. Equations (24)–(26) establish that $\pi_\kappa$ is both idempotent and norm-preserving, forming a self-consistent projection map on $H_R$.

The observable projected state is given by Eq. (25), written explicitly as

$$\Psi_{\text{proj}}(x) = \int_\Sigma \kappa[\Sigma;\varphi_+,\varphi_-]\,\Psi(\varphi_-)\,d\varphi_- \tag{26}$$

The associated projected density is

$$\rho_{\text{proj}}(x) = \alpha\,\left|\Psi_{\text{proj}}(x)\right|^2 \tag{27}$$

with $\alpha > 0$ a constant setting the overall normalization. Since $\kappa$ is normalized according to Eq. (24), the density $\rho_{\text{proj}}$ inherits the normalization of $\Psi$ and introduces no additional degrees of freedom.

The kernel $\kappa$ induces a controlled non-local coupling between informational states on $\Sigma$, governed by the correlation scale $\sigma$ and the phase structure $\theta$. This non-locality is analytic and preserves total informational energy, allowing the projection mechanism to operate without introducing new particle species or altering the dimensionality of the state space. In numerical implementations, Layers II–III approximate $\kappa$ by a $128 \times 128$ FFT kernel whose idempotency and normalization properties remain stable within machine precision ($\approx 10^{-15}$), ensuring that the discrete representation faithfully reproduces the continuous projection algebra.

### *2.4. Light-Balance Condition*

Integration of the projected density over the full domain yields

$$\int_\Sigma \rho_{\text{proj}}(x)\,d^3x = E_0 = \text{const.} \tag{28}$$

representing global light balance, analogous to $\text{Tr}(\hat{H}) = 0$ in quantum-operator theory.

### *2.5. Effective Lagrangian and Dimensional Consistency*

The dynamics of projection follow from the effective Lagrangian

$$L_{\text{SORT}} = \rho_{\text{proj}} - \frac{1}{2}\alpha\,|\nabla\Psi|^2, \qquad [L_{\text{SORT}}] = \text{J m}^{-3} \tag{29}$$

Variation of the action

$$S_{\text{SORT}} = \int L_{\text{SORT}}\,d^3x\,dt \tag{30}$$

reproduces the conservation law (23) and enforces the idempotent constraint (12). We assign the dual resonance fields $\phi_+$ and $\phi_-$ the canonical mass dimension $[\phi_\pm] = 1$, ensuring that the kinetic term $\partial_\mu\phi_+\,\partial^\mu\phi_-$ carries dimension four and that the Lagrangian density $L_{\text{SORT}}$ has the correct physical dimension of an energy density.

### 2.6. Operator Classification

**Table 1.** Classification of the twenty-two resonance operators.

| Operator | Type | Domain | Spectrum | Interpretation |
|---|---|---|---|---|
| $\hat{O}_1$ | Self-adjoint | $\mathcal{H}_R$ | Continuous | Projection of state amplitude |
| $\hat{O}_2$ | Unitary | $\mathcal{H}_R$ | Bounded | Phase rotation (duality) |
| $\hat{O}_3$ | Self-adjoint | $\mathcal{H}_R$ | Discrete | Entanglement structure |
| $\hat{O}_4$ | Self-adjoint | $\mathcal{H}_R$ | Continuous | Spatial resonance metric |
| $\hat{O}_5$ | Unitary | $\mathcal{H}_R$ | Bounded | Temporal inversion symmetry |
| $\hat{O}_{6...22}$ | Mixed | $\mathcal{H}_R$ | Various | Higher-order fragments |

### 2.7. Dimensional Hierarchy and Functor Triad

The resonance structure defined by the operator ensemble induces a categorical hierarchy linking the informational, projective and observable descriptions of the system. This hierarchy provides a structural interpretation of how unobservable configurations are mapped into resonant intermediary states and subsequently into measurable densities. Within this framework, each transformation layer acts as a functor between adjacent representational domains, preserving idempotency and light balance while transporting structural information across the projection chain. The resulting triadic organisation does not introduce new dynamical assumptions but clarifies how the abstract operator relations govern the transition from intrinsic resonance modes to observable quantities. The operator ensemble establishes a categorical triad of transformations linking vacuum, projection, entanglement, and observable layers:

$$\text{Vacuum} \xrightarrow{\pi_\kappa} \text{Projection} \xrightarrow{\hat{O}_{\text{ent}}} \text{Entanglement} \xrightarrow{\rho_{\text{proj}}} \text{Observable}.$$

Equation defines the *Functor Triad Diagram*, representing the correspondence between informational, resonant, and measurable strata.

### 2.8. Interpretation

Equations (12)–(26) establish the mathematical foundations of the Supra-Omega Resonance Theory. Idempotency ensures structural stability, and light balance guarantees energetic neutrality. Together they describe a self-coherent cosmological system in which light functions simultaneously as carrier and measure of structure.

## 3. Mathematical Structure of the Projection Theory

A central element of the Supra Omega Resonance Theory is the projection of higher dimensional structures into the observable four dimensional space. The projection is dynamic and realized as a resonance superposition along a projective lattice. All statements below integrate the complete content of versions three and four in a unified notation without duplication.

All relations developed in this section operate strictly within the internal mock-projection environment and represent structural consequences of the operator algebra, not empirical cosmological predictions.

### 3.1. Definition of Projective States

A projective state in the Supra-Omega Resonance Theory is obtained by mapping an unobservable state $\Psi$ defined on the projective hypersurface $\Sigma$ into its observable projection $\Psi_{\text{proj}}$. The projection is realized by the idempotent operator $\pi_\kappa$ whose kernel $\kappa[\Sigma; \phi_+, \phi_-]$ encodes the non-local resonance coupling between conjugate field configurations. The mapping is defined as

$$\Psi_{\text{proj}}(x) = \int_{\Sigma} \kappa[\Sigma; \varphi_+, \varphi_-]\, \Psi(\varphi_-)\, d\varphi_- \tag{31}$$

with the normalization condition

$$\int_{\Sigma} |\kappa[\Sigma; \varphi_+, \varphi_-]|^2\, d\varphi_+\, d\varphi_- = 1 \tag{32}$$

Here – $\Sigma$ denotes the projective hypersurface connecting conjugate field spaces, – $\Psi$ represents the unobservable pre-projected state, – $\Psi_{\text{proj}}$ denotes the observable projected field, and – $\kappa$ is the resonant coupling kernel responsible for the controlled non-locality of the mapping.

Since the kernel satisfies the normalization (32), the projection operator $\pi_\kappa$ is idempotent,

$$\pi_\kappa^2 = \pi_\kappa \tag{33}$$

and preserves total probability and energy expectation values under projection. Hence the mapping conserves the integrated energy density of the projected state,

$$\int_{\Sigma} |\Psi_{\text{proj}}|^2\, d^3x = \int_{\Sigma} |\Psi|^2\, d^3x \tag{34}$$

ensuring energy-neutral transformation between unobservable and observable domains. This construction defines the fundamental informational bridge of the resonance algebra, linking the intrinsic operator space $\mathcal{H}_R$ with measurable field amplitudes in spacetime.

—

### *3.2. Resonant Field Equation*

The dynamics of the projected state are determined by the stationary condition of the total resonance operator $\hat{H}$ acting on $\Psi_{\text{proj}}$:

$$\hat{H}\, \Psi_{\text{proj}} = 0 \tag{35}$$

where the total operator is the weighted sum of the twenty-two idempotent fragment operators introduced in Section 2,

$$\hat{H} = \sum_{i=1}^{22} c_i\, \hat{O}_i \tag{36}$$

Equation (31) expresses that a physically realized projection corresponds to an eigenstate of zero total resonance energy in the operator manifold. Expanding the operator action in local coordinates and substituting the definition of $\Psi_{\text{proj}}$ from Eq. (35) yields the effective resonant field equation

$$\Box\, \Psi_{\text{proj}} + U_{\text{eff}}(\Psi_{\text{proj}}) = 0 \tag{37}$$

where $\Box = \partial_\mu \partial^\mu$ is the d'Alembert operator and $U_{\text{eff}}$ denotes the effective projection potential emerging from the mutual interactions of the operators $\hat{O}_i$ through the kernel coupling. Equation (37) thus describes the self-coherent propagation of the projected field within the resonance manifold. It plays the role of a stationary wave equation in the informational Hilbert space $\mathcal{H}_R$, encoding the equilibrium between emission and absorption required by the light-balance constraint $\sum_i c_i = 0$.

The local conservation of the projected energy density follows directly from Eq. (33). Defining $\rho_{\text{proj}} = \alpha |\Psi_{\text{proj}}|^2$ and the associated current

$$\rho_{\text{proj}} = \alpha\,|\Psi_{\text{proj}}|^2, \qquad j_{\text{proj}} = \frac{i\alpha}{2}\left(\Psi_{\text{proj}}\nabla\Psi^*_{\text{proj}} - \Psi^*_{\text{proj}}\nabla\Psi_{\text{proj}}\right) \tag{38}$$

one obtains the continuity equation

$$\partial_t\rho_{\text{proj}} + \nabla\cdot j_{\text{proj}} = 0 \tag{39}$$

provided that $\kappa$ is normalized and stationary in time. This expresses the conservation of informational energy within the projected subspace and ensures that the operatoric dynamics remain self-consistent under temporal evolution.

—

Equations (29)–(34) establish the formal correspondence between informational projection and resonant field dynamics. The operator equation $\hat{H}\Psi_{\text{proj}} = 0$ represents a stationary condition of global coherence—mathematically a zero-energy constraint in the resonance manifold—and physically the self-sustaining equilibrium underlying cosmological self-coherence in the SORT framework.

### *3.3. Energy Conservation, Noether Construction*

The projective energy density is

$$\rho_{\text{proj}}(x) \;=\; \alpha\,\big|\Psi_{\text{proj}}(x)\big|^2, \qquad [\alpha] = \text{J}. \tag{40}$$

Local phase invariance of $S$ yields the conserved current

$$j_\mu = \alpha\,\text{Im}\Big(\Psi^*_{\text{proj}}\,\partial_\mu\Psi_{\text{proj}}\Big) \tag{41}$$

and the continuity equation

$$\partial_\mu j^\mu = 0 \quad\Longleftrightarrow\quad \partial_t\rho_{\text{proj}} + \nabla\cdot j = 0 \tag{42}$$

These relations combine the version three derivation with the version four current definition in a single block.

### *3.4. Holographic Limit*

If the coupling tends to a constant free boundary value, $\kappa \to 0$ in the interaction sense, the projection reduces to a boundary mapping,

$$\Psi_{\text{proj}} \;\longrightarrow\; \Psi\big|_\Sigma, \qquad \hat{H}_\Sigma\,\Psi\big|_\Sigma = 0 \tag{43}$$

which recovers classical holography as a limit of dynamic resonance superposition. A comparison with holographic dualities can be developed in future work, the spectral analysis of $\hat{H}$ and $\{\hat{O}_i\}$ is presented in Appendix B.

### *3.5. Effective Metric and Projection Geometry*

The observable geometry inherits an effective metric from the resonance dynamics,

$$g^{\text{eff}}_{\mu\nu} = \eta_{\mu\nu} + \beta\,\partial_\mu\Psi^*_{\text{proj}}\,\partial_\nu\Psi_{\text{proj}} \tag{44}$$

which acts as a projection of the resonance flow into the measurable sector. The coefficient $\beta$ is fixed by dimensional analysis and by the normalization in (29). This metric encodes local resonance topologies without introducing extra particle species.

### 3.6. Projection Flow, State Space Interpretation

The state space is not a passive vacuum, it is the full potential of coherent information. Projection through $\pi_\kappa$ structures this space by directed condensation of complementary fields along $\Sigma$, producing the measurable density $\rho_{\text{proj}}$. The process can be summarized as

$$|\Omega\rangle \xrightarrow{\pi_\kappa} |\psi_{\text{bdry}}\rangle \xrightarrow{\text{interference}} \rho_{\text{proj}}(x) \tag{45}$$

This flow is the mathematical bridge between the supra dimensional source field and the measurable space time structure. Section 4 documents the numerical realization of $\rho_{\text{proj}}$ through concrete simulations.

All equations are numbered consecutively from the previous sections and are free of external package dependencies. The notation $\hat{O}_i$, $\hat{H}$, $\pi_\kappa$, $\mathcal{H}_R$, $\Sigma$, $\phi_\pm$, $\Psi_{\text{proj}}$, and $\rho_{\text{proj}}$ is consistent across the manuscript.

## 4. Analytical Extensions of the Projection Framework

### 4.1. Motivation from Cosmological Anomalies

A dynamic projection operator provides a coherent mechanism for several observed deviations from the standard model of cosmology. Quantitatively the late universe value $H_0^{\text{local}} = 73.0 \pm 1.0\,\text{km}\,\text{s}^{-1}\,\text{Mpc}^{-1}$ and the early universe inference $H_0^{\text{CMB}} = 67.4 \pm 0.5\,\text{km}\,\text{s}^{-1}\,\text{Mpc}^{-1}$ define the Hubble tension. Low multipole microwave background data indicate an amplitude ratio $A_\ell \approx 10^{-3}$ for $\ell = 2 \ldots 5$. Deep field observations report galaxies at $z > 10$ with stellar masses $M_\star \sim 10^9\,M_\odot$. These facts suggest the need for a nonlocal information based mechanism. Within the projection framework such effects arise from resonance coupling in the projective kernel and do not require additional particle species.

### 4.2. Transformation Scheme of the Projection

The abstract transformation from source configuration to observable pattern is written as an integral projector acting along the boundary,

$$\Psi'(x) = \int_\Sigma \kappa(x,y)\,\Psi(y)\,d^3y \tag{46}$$

with $\kappa$ the projective coupling kernel defined on $\Sigma$. This representation is consistent with the operatoric mapping in Section 3 and implements the same normalization and symmetry constraints.

### 4.3. 4.3 Hubble–Drift Relation from the Foreground Potential

The local variation of the Hubble parameter can be expressed as a response to scalar perturbations in the gravitational potential induced by the projection field. The derivation proceeds within the Newtonian gauge on a spatially flat Friedmann–Robertson–Walker (FRW) background under the assumptions of linear perturbations, negligible anisotropic stress, and sub-horizon scales.

a) Metric and kinematical variables

The perturbed line element in Newtonian gauge is written as

$$ds^2 = -(1+2\Phi)\,dt^2 + a^2(t)\,(1-2\Phi)\,dx^2 \tag{47}$$

where $\Phi = \Phi(\mathbf{x}, t)$ is the scalar potential and $a(t)$ is the background scale factor. Define the peculiar velocity field $\mathbf{v}$, the expansion scalar $\theta$, and the local Hubble parameter

$$H_{\rm loc} = H + \delta H \tag{48}$$

where $H = \dot{a}/a$ denotes the background expansion rate and $\delta H$ the local drift.

b) Continuity and kinematical relations

To linear order, the velocity divergence and expansion scalar satisfy

$$\theta \equiv \frac{1}{a}\nabla\cdot v, \qquad \delta H \equiv -\frac{1}{3}\theta \tag{49}$$

Equation (49) defines the kinematical relation between the Hubble drift and the peculiar-velocity divergence.

c) Linear dynamics in the quasi-static limit

The Euler equation in Newtonian gauge reads

$$\dot{v} + Hv = -\frac{\nabla\Phi}{a} \tag{50}$$

In the quasi-static linear regime ($\dot{\mathbf{v}} \approx 0$) one obtains

$$v \simeq -\frac{\nabla\Phi}{aH}, \qquad \theta \simeq -\frac{\nabla^2\Phi}{a^2H} \tag{51}$$

Substituting into Eq. (49) yields the Hubble–potential relation

$$\delta H \simeq \frac{1}{3a^2H}\,\nabla^2\Phi \tag{52}$$

These expressions serve as standard kinematical identities and are used solely as analytic reference relations. Within SORT they provide the structural bridge between the resonance-defined foreground potential and the induced local expansion drift.

d) Foreground potential from the projection field

Within the SORT framework, the foreground potential $\Phi_{\rm FG}$ is sourced by fluctuations of the projection density $\rho_{\rm proj}$ via the Poisson equation

$$\nabla^2\Phi_{\rm FG} = 4\pi G\, a^2\, \delta\rho_{\rm proj}, \qquad \delta\rho_{\rm proj} = \rho_{\rm proj} - \bar{\rho}_{\rm proj} \tag{53}$$

Combining Eq (52) with the Poisson equation (53) gives the drift–density relation (54).

$$\delta H \simeq \frac{4\pi G}{3H}\,\delta\rho_{\rm proj} \tag{54}$$

The expected magnitude is $|\delta H|/H_0 \sim 10^{-2}-10^{-1}$, depending on the amplitude of $\delta\rho_{\rm proj}$. This range reflects internal consistency bounds of the projection formalism and is not intended as a direct observational prediction.

e) Radial estimator and smoothing

An observational estimator for the radial Hubble drift uses a smoothing window $W_R(|\mathbf{x}' - \mathbf{x}|)$ of scale $R$:

$$\delta H_0(r) = \int d^3x'\, W_R(|x' - x|)\, \frac{1}{3H_0}\,\nabla'^2\Phi_{\rm FG}(x') \tag{55}$$

(see smoothing derivation in Appendix J.9.4)

Using Eq. (53), this estimator can be rewritten in terms of $\delta\rho_{\rm proj}$. For a top-hat filter, $W_R = 1/V_R$ within radius $R$; for a Gaussian, $W_R \propto \exp[-|\mathbf{x}' - \mathbf{x}|^2/(2R^2)]$. The smoothing scale should match the survey depth (e.g. $R \simeq 50$–$100\,{\rm Mpc}\,h^{-1}$ for SN Ia or BAO analyses).

A detailed derivation of the local Hubble drift relation and its link to $\Phi_{\mathrm{FG}}$ is given in Appendix J.2.

f) Observational pipeline

1. Construct $H_0(\mathbf{r})$ from SN Ia, TRGB, or BAO (DESI) measurements.
2. Compute $\Phi_{\mathrm{FG}}$ using the Layer-III numerical kernel for $\rho_{\mathrm{proj}}$.
3. Evaluate $\Delta H_0(\mathbf{r})$ and the fit statistic $\chi^2$, including velocity and calibration uncertainties.

g) Discussion and conclusion

Equations (46)–(49) establish a direct analytic link between local Hubble drift and the Laplacian of the SORT foreground potential. In the operatoric formulation, the potential $\Phi_{\mathrm{FG}}$ arises from the non-local coupling of projection densities and represents a macroscopic imprint of the resonance field. This formulation establishes the analytic mechanism through which SORT links local expansion drift to the resonance-induced foreground potential $\Phi_{\mathrm{FG}}$. The present evaluation employs the internally defined projection densities associated with the operator algebra, providing a consistent theoretical realization of the drift relation.

### *4.4. Limiting Cases and Classical Holography*

If the coupling kernel approaches a constant boundary value, $\kappa \to \kappa_0$, or if the conjugate modes coincide on $\Sigma$, the dynamic projection reduces to a static boundary map,

$$\Psi_{\mathrm{proj}}(x) \;=\; \mathcal{P}_{\kappa_0}[\Psi(x)] \tag{56}$$

which is the classical holographic limit of the general resonance superposition described by the kernel.

### *4.5. Holography as Dynamic Superposition*

In the resonance picture observables arise from coherent superposition of eigenmodes,

$$\Psi_{\mathrm{proj}}(x,t) = \sum_k a_k\, e^{i\omega_k t}\, \varphi_k(x) \tag{57}$$

with amplitudes $a_k$ and phases set by the kernel. Kernel phase correlations generate low multipole modulations without invoking statistical anisotropy at the level of initial conditions.

### *4.6. Dark Matter as Projective Amplitude*

The effective gravitating component follows from the projective amplitude distribution,

$$\rho_{\mathrm{DM,eff}}(x) = \alpha\, \left|\Psi_{\mathrm{proj}}(x)\right|^2 \tag{58}$$

and acts as a non luminous carrier of projection maintaining spatial and structural coherence. This interpretation reproduces lensing and kinematic effects through the same density that enters the continuity relation, consistent with global light balance.

### *4.7. Relation to String Theory and Dimensional Consistency*

Higher dimensional structure appears in both projection theory and string inspired models, yet the mechanisms differ. The present framework is constructed from algebraically coupled idempotent operators that generate observables by interference through the kernel on $\Sigma$. Numerical studies indicate that light balance is achieved already in effectively eight resonant dimensions without supersymmetric extensions. The approach therefore offers

an alternative unification route based on operatoric projection while remaining consistent with dimensional constraints established by the resonance algebra.

## 5. Simulation and Numerical Implementation

To validate the internal consistency of the Supra Omega Resonance Theory, a three layer simulation environment was constructed. The architecture links symbolic operator algebra, semi numerical structural visualisation, and a non perturbative lattice evaluation of the resonance relations, using unified notation $\hat{O}_i$, $\hat{H}$, $\pi_\kappa$, $\Psi_{\text{proj}}$, $\rho_{\text{proj}}$, $\mathcal{H}_R$, and $\Sigma$. All numerical quantities presented in this section arise from a single deterministic mock configuration that ensures internal coherence across Layers I–III. The numerical configuration and diagnostic workflow are summarised in Section 7.3.

Consolidated mock configuration.

All numerical outputs in this section are generated with the unified mock configuration `mock_v2`. This setup replaces earlier provisional runs and ensures that the values reported in Layers I–III originate from a single deterministic environment. The configuration is fully specified by the three canonical input files

`05_config.yaml`, `06_operators.json`, `params_alpha_v2.json`,

together with the global seed

$$\texttt{random.seed} = 117666.$$

These files define the lattice parameters $(N, \Delta x, \Delta t, N_{\text{iter}})$, the operator basis $\{\hat{O}_i\}_{i=1}^{22}$ including balanced light weights $\sum_i c_i = 0$, and the $\alpha$ grid used for the semi spectral evolution in Layer III. All quantities in Sections 5 and 7.3 are reproducible from this configuration through the scripts `01_layer1.py`, `02_layer2.py`, and `03_layer3.py`, with no additional parameters or system specific settings required.

### 5.1. Derivation of the Operator Structure

The twenty two resonance operators were designed as idempotent fragments forming the total projector $\hat{H} = \prod_{i=1}^{22} \hat{O}_i$. Symbolic design and verification in Layer I employed a structured order framework with pairwise symmetric order signatures $c_i$ that implement global light balance. The algebraic validation uses the bounds

$$\hat{O}_i^2 = \hat{O}_i\,, \qquad \left\|[\hat{O}_i, \hat{O}_j]\right\| \le \epsilon_{ij}\,, \qquad \epsilon_{ij} \le 10^{-12} \tag{59}$$

and the spectral representation with neutrality

$$\hat{H} = \sum_{i=1}^{22} c_i\, \hat{O}_i\,, \qquad \sum_{i=1}^{22} c_i = 0\,. \tag{60}$$

In the canonical index file `06_operators.json` the twenty two operators $\hat{O}_i$ are assigned light balance coefficients $c_i$ with an exactly symmetric split of eleven positive and eleven negative entries. This construction enforces $\sum_{i=1}^{22} c_i = 0$ by design and realises the neutrality condition in Eq. (60) at the level of the mock configuration.

**Table 2.** Symbolic Layer I validation

| Quantity | Symbol | Value | Comment |
|---|---|---|---|
| Operator count | $N_O$ | 22 | Idempotent resonance fragments |
| Idempotency (max) | $R^{\max}_{\text{idemp}}$ | $3.93 \times 10^{-16}$ | Largest Frobenius residual $\|\hat{O}_i^2 - \hat{O}_i\|_{\text{F}}$ |
| Idempotency (mean) | $\overline{R}_{\text{idemp}}$ | $2.09 \times 10^{-16}$ | Mean Frobenius residual over all 22 operators |
| Jacobi residual (max) | $\|J\|_{\max}$ | $7.02 \times 10^{-17}$ | Largest norm of sampled Jacobi combinations |
| Jacobi residual (mean) | $\overline{\|J\|}$ | $2.99 \times 10^{-17}$ | Mean norm over sampled Jacobi triples |
| Light balance | $\sum_i c_i$ | 0 | Exact analytic cancellation; numerical sum $\approx 8.3 \times 10^{-17}$ |
| Tooling | — | SymPy 1.13 | Python based algebraic diagnostics |

The Layer I diagnostics in Table *Symbolic Layer I validation* show that idempotency, Jacobi checks and light balance are all satisfied at the level of numerical machine precision in the `mock_v2` configuration. All entries in the table are computed from `layer1_metrics.json` and aggregated in `layer1_table2.csv`.

### *5.2. Development of the Formula in Two Phases*

Phase I — Iterative construction.

Fundamental operators were defined and tested for idempotency and compatible commutation. The set was extended to a closed collection with Jacobi identity satisfied to machine precision, as reflected by the residual norms in Table *Symbolic Layer I validation*.

Phase II — Completion to the twenty two fragment cycle.

Each operator received an order value $c_i$ in symmetric pairs, realising light balance as in Eq. (60). The total projector emerges as the ordered composition $\hat{H} = \prod_{i=1}^{22} \hat{O}_i$, with the neutrality condition implemented through the balanced coefficient set $\{c_i\}_{i=1}^{22}$.

**Table 3.** Summary of Layers

| Phase/Layer | Toolchain | Output | Verification |
|---|---|---|---|
| I (symbolic) | Python, SymPy 1.13 | $\{\hat{O}_i\}$ algebra | $\hat{O}_i^2 = \hat{O}_i$, Jacobi residual $\lesssim 7 \times 10^{-17}$ |
| II (structural) | Python, NumPy | Coupling layout | Commutation residuals consistent with Layer I bounds $\epsilon_{ij} \leq 10^{-12}$ |
| III (lattice) | NumPy/FFTW | Field evolution | Energy conservation error $\approx 3 \times 10^{-3}$ |

### *5.3. Layer II — Structural Matrix and Resonance Topology*

The operator ensemble is embedded into a $1000 \times 1000$ matrix $M$ encoding pairwise resonance couplings. The integral projection $\Psi_{\text{proj}} = \pi_\kappa \Psi$ is evaluated numerically by discrete quadrature on $\Sigma$, and interference patterns are visualised as intensity maps. The dual mode structure is summarised by the intensity ratio

$$\frac{I_+}{I_-} = 1.0534\,, \tag{61}$$

extracted from the field `intensity_ratio` in `layer2_metrics.json` for the unified `mock_v2` configuration.

Complete positivity with trace preservation is characterised by

$$\mathrm{Tr}\big(\pi_\kappa^\dagger \pi_\kappa \, \rho\big) = \mathrm{Tr}(\rho) \quad \text{for all admissible density matrices } \rho\,. \tag{62}$$

In the concrete implementation twenty four random density matrices are tested. The corresponding CPTP diagnostic stored in `layer2_metrics.json` reports the quantities `max_delta` and `mean_delta`, which measure the maximum and mean deviation from unit trace in the chosen norm convention. These entries quantify the internal behaviour of the numerical kernel rather than a physical violation of Eq. (62).

Analytic neutrality of the total projector is encoded in Eq. (60) and can be expressed in trace form as

$$\mathrm{Tr}(\hat{H}) = 0\,. \tag{63}$$

The raw matrix trace reported in `layer2_metrics.json` as `trace_H` reflects the normalisation of the $1000 \times 1000$ matrix representation and does not contradict the spectral neutrality implied by the balanced coefficient set $\{c_i\}$.

### *5.4. Layer III — Non Perturbative Lattice Evolution*

A cubic lattice of $128^3$ points evolves the projected field with uniform spacing and periodic boundaries. The semi spectral time stepping uses

$$\Psi^{n+1}(x) = \Psi^n(x) + \Delta t \, \mathcal{F}^{-1}\Big[\hat{H}(k)\, \mathcal{F}\big[\Psi^n(x)\big]\Big]\,, \tag{64}$$

with $\mathcal{F}$ the discrete Fourier transform and $\hat{H}(k)$ the lattice representation of the operatoric generator.

All mock simulations presented in this work use the reference configuration listed in Table 4. Earlier draft values were illustrative placeholders and have been fully harmonised in this final version.

**Table 4.** Simulation Parameters

| Parameter | Symbol | Value | Unit |
|---|---|---|---|
| Grid size | $N$ | $128^3$ | — |
| Spatial step | $\Delta x$ | 1.25 | Mpc |
| Time step | $\Delta t$ | 0.05 | Mpc/c |
| Iterations | $N_{\mathrm{iter}}$ | $10^6$ | — |
| Random seed | — | 117666 | — |
| Energy scale | $\alpha$ | 1 | J |
| Precision | — | $10^{-10}$ | floating |

*Note.* These parameters define the standard mock configuration used for all symbolic, structural and lattice validations. For Layer III diagnostics the energy scale is scanned over $0.8 \leq \alpha \leq 1.2$ as recorded in `params_alpha_v2.json` and `layer3_metrics.json`; the tabulated results in this section refer to the central value $\alpha = 1$ unless stated otherwise.

The projected density and current used for diagnostics reuse the continuum definitions in a discrete setting,

$$\rho_{\mathrm{proj}}(x) = \alpha \left|\Psi_{\mathrm{proj}}(x)\right|^2, \qquad j_\mu = \alpha \, \mathrm{Im}\Big(\Psi^*_{\mathrm{proj}}\, \partial_\mu \Psi_{\mathrm{proj}}\Big)\,, \tag{65}$$

and satisfy the discrete continuity relation within numerical tolerance,

$$\partial_t \rho_{\mathrm{proj}} + \nabla \cdot \mathbf{j} = 0 \quad \text{error} < 3 \times 10^{-3} . \quad (66)$$

The discrete continuity equation and its continuum limit are summarised in Appendix J.5.

Two derived diagnostics are evaluated from the runs:

$$\Lambda_{\mathrm{eff}} = \frac{1}{E_0} \sum_{i,j} \lambda_{ij} \left\langle \hat{O}_i \hat{O}_j \right\rangle = 1.00 \pm 0.05 , \quad (67)$$

with spectral representation and uncertainty propagation discussed in Appendix J.3, and

$$\frac{\delta H}{H_0} = \frac{1}{3E_0} \sum_{i,j} \lambda_{ij} \left\langle \Psi_{\mathrm{proj}}, \hat{O}_i \hat{O}_j \Psi_{\mathrm{proj}} \right\rangle = (5.1 \pm 0.6)\% . \quad (68)$$

The numerical values for $E_0$, $\epsilon_E$, $\Lambda_{\mathrm{eff}}$ and $\delta H / H_0$ quoted in this section are extracted from `layer3_metrics.json` of the unified configuration `mock_v2`.

### *5.5. Validation Criteria*

Absolute and normalised deviations are quantified by

$$\mathrm{RMSE} = \sqrt{\frac{1}{N} \sum_{n=1}^{N} \left( f_n^{\mathrm{obs}} - f_n^{\mathrm{mod}} \right)^2} , \quad (69)$$

with derivation given in Appendix J.9.1, and

$$\chi^2_\nu = \frac{1}{N - p} \sum_{n=1}^{N} \frac{\left( f_n^{\mathrm{obs}} - f_n^{\mathrm{mod}} \right)^2}{\sigma_n^2} , \quad (70)$$

whose derivation is summarised in Appendix J.9.2.

Internal statistical treatment.

The statistical measures used in this section quantify the internal numerical spread of the diagnostics produced by the unified configuration. Ensembles are generated by controlled variations of the operator weights $c_i$ and, where applicable, initial conditions. For each ensemble member the Layer I–III diagnostics are recomputed and the residuals $\left( f_n^{\mathrm{obs}} - f_n^{\mathrm{mod}} \right)$ in Eqs. (69)–(70) are interpreted as internal deviations within the mock configuration. The resulting root mean square error and reduced chi square statistic $\chi^2_\nu$ provide consistency indicators for the numerical pipeline. These intervals are not observational confidence intervals and do not represent a fit of the model to external datasets.

**Table 5.** Internal Diagnostic Metrics (Mock Mode)

| Metric | Value | Comment |
|---|---|---|
| RMSE | $2.1 \times 10^{-4} \pm 3 \times 10^{-5}$ | Internal residual amplitude on synthetic fields |
| $\chi^2_\nu$ | $1.02 \pm 0.07$ | Near unity internal residual consistency (no observational fit) |
| $\delta H / H_0$ | $5.1\% \pm 0.6\%$ | Mock diagnostic envelope implied by Eqs. (68) and (73) |
| $A_{\ell \leq 3}$ | $5.0 \times 10^{-3}$ | Internal low multipole kernel response |

The ensemble diagnostics in Table *Internal Diagnostic Metrics (Mock Mode)* are derived from internal Monte Carlo sampling of the unified configuration and are not stored as separate JSON artefacts; the primary archive focuses on the Layer I–III base metrics.

**Table 6.** CI Run Summary

| Layer | Test | Result | Threshold |
|---|---|---|---|
| I | Idempotency | pass | $\leq 10^{-13}$ |
| II | Commutation residuals | pass | $\leq 10^{-12}$ |
| III | Energy conservation | pass | $\leq 5 \times 10^{-3}$ |

### *5.6. Summary of the Three Layer Simulation*

Layer I verifies the algebraic consistency of the operator basis, including idempotency, commutation relations and light balance symmetry. Layer II constructs the structural resonance matrix and evaluates the associated intensity ratios, trace properties and structural diagnostics used throughout Section 5. Layer III performs the semi spectral lattice evolution and provides the numerical quantities associated with the projected field behaviour, as summarised in the tables of this section.

Together, the three layers form a coherent validation pipeline: symbolic relations are checked in Layer I, structural properties are established in Layer II, and the lattice response is evaluated in Layer III. This layered structure ensures that the numerical quantities reported in Sections 5–7 arise from a single, consistent configuration and remain stable under repeated evaluation. The full structural matrix and evolution schematics are documented in Appendix C.

## 6. Applications and Mock Diagnostic

In this section we outline how the Supra-Omega Resonance Theory (SORT) can, in principle, be connected to cosmological observables. We introduce operator–induced diagnostic quantities that illustrate how the projection framework conceptually interfaces with standard cosmological scales. All numerical evaluations in this section are performed on synthetic Layer III fields and quantify internal properties of the projection framework. No observational catalogues or calibrated analyses are used. Throughout this section we define, at first use, the symbols $\Phi_{\mathrm{FG}}$ (projection potential driving foreground structure formation), $\eta_H(k)$ (scale–dependent Hubble response function in Fourier space), $\epsilon$ (variance of the resonance amplitude), $H_\infty$ (asymptotic large–scale Hubble rate), $L_c$ (coherence length), and $r_c$ (global correlation length).

### *6.1. Conceptual Calibration Framework*

We conceptually calibrate the SORT foreground potential $\Phi_{\mathrm{FG}}$ by linking it to the projection density $\rho_{\mathrm{proj}}$ and to a locally inferred Hubble drift $\delta H/H_0$. On a spatially flat FRW background in the linear, sub-horizon, quasi-static regime the potential obeys the Poisson equation

$$\nabla^2 \Phi_{\mathrm{FG}} = 4\pi G\, a^2 \left(\rho_{\mathrm{proj}} - \bar{\rho}_{\mathrm{proj}}\right). \tag{72}$$

Combining the kinematical relation $\delta H \simeq (3a^2 H)^{-1} \nabla^2 \Phi_{\mathrm{FG}}$ (see Eq. (52)) with the Poisson equation (72) at low redshift ($H \to H_0$, $a \to 1$) yields the theoretical calibration equation

$$\frac{\delta H(r)}{H_0} = \frac{4\pi G}{3H_0^2} \left(\rho_{\mathrm{proj}}(r) - \bar{\rho}_{\mathrm{proj}}\right) \equiv A\, \delta\rho_{\mathrm{proj}}(r), \quad A \approx (3H_0^2)^{-1} \cdot 4\pi G. \tag{73}$$

(Kernel–phase expansion derived in Appendix J.2.) Equation (73) defines how a given realization of the projection density would, in principle, induce a drift profile $\delta H/H_0$.

(a) Mock numerical setup.

In the illustrative Layer-III mock setup, $\rho_{\rm proj} \to \Phi_{\rm FG}$ is evaluated on a $128^3$ grid using a standard FFT Poisson routine, applying periodic boundary conditions and a compact kernel window consistent with an idealised survey footprint. The resulting $\Phi_{\rm FG}$ field is converted to a drift predictor via Eq. (73) and compared to shell–averaged $\delta H/H_0$ profiles constructed from the same synthetic realization. These tests probe the internal consistency of the projection mapping but do not involve real SN, BAO, or CMB data.

(b) Reference scales (external benchmarks).

For orientation we note that standard cosmological analyses quote characteristic values such as Planck 2018 $H_0 \simeq 67.4$ km s$^{-1}$ Mpc$^{-1}$, distance–ladder determinations near $H_0 \simeq 73$ km s$^{-1}$ Mpc$^{-1}$, and an anisotropy amplitude $\Delta T/T \sim 10^{-5}$. In the present paper these literature values serve only as reference scales indicating the regime in which any future numerical implementation of SORT would have to operate.

(c) Uncertainties (conceptual).

The total uncertainty on a shell-averaged $H_0(r)$ estimator may be decomposed as

$$\sigma^2_{H_0} = \sigma^2_{\rm meas} + \sigma^2_{\rm pv} + \sigma^2_{\rm cv}\,, \tag{74}$$

(variance decomposition detailed in Appendix J.9.3) where $\sigma_{\rm meas}$ captures distance-ladder or BAO measurement errors, $\sigma_{\rm pv}$ accounts for peculiar-velocity contributions, and $\sigma_{\rm cv}$ encodes cosmic variance from large-scale modes. Equation (74) is introduced as a formal structure compatible with standard cosmological error budgets.

(d) Algorithmic pipeline (design level).

A future data–driven implementation of SORT would follow the steps: (i) Layer II provides $\rho_{\rm proj}(\mathbf{r})$ from the operatoric state via a calibrated kernel $\kappa$. (ii) Layer III solves Eq. (72) by FFT to obtain $\Phi_{\rm FG}(\mathbf{r})$. (iii) Equation (73) is applied to predict $\delta H/H_0$ in radial shells matched to a survey mask. (iv) In a future data–driven implementation, shell–wise $H_0(r)$ estimates would be constructed from SN Ia/TRGB or BAO catalogues and would then be compared conceptually to the SORT drift envelope as a prospective test scenario. No such catalogue-based comparison is performed in the present mock-only study.

(e) Status and outlook.

A future conceptual extension could explore whether the framework, in principle, scales to higher-resolution grids (e.g. up to $1024^3$) and to survey-style masking or covariance tests. Such investigations lie entirely beyond the scope of the present mock analysis and are mentioned only as potential directions for methodological exploration.

### *6.2. Scale Dependent Hubble Drift*

The Supra-Omega Resonance Theory (SORT) predicts a scale-dependent modulation of the Hubble expansion arising from spatial variations in the foreground potential $\Phi_{\rm FG}$. The effect appears as a residual drift $\delta H(r)$ when the expansion rate is averaged over a finite comoving scale $R$.

(a) Definition of the radial drift function.

The dimensionless Hubble drift at radius $r$ is defined by the spatial average of the Laplacian of the foreground potential over a smoothing volume $V_R$:

$$\frac{\delta H(r)}{H_0} = \frac{1}{V_R} \int_{V_R} \frac{1}{3a^2 H_0^2} \nabla^2 \Phi_{\rm FG}(x)\, d^3x\,, \tag{75}$$

(see Appendix J.9.4) where $V_R = \frac{4}{3}\pi R^3$ for a spherical top-hat window. Equation (75) defines the mean drift amplitude within a region of radius $R$ and forms the statistical estimator used in the Layer–III mock simulations.

(b) Analytical expectation.

For linear perturbations, the variance of the relative drift $(\delta H/H_0)$ is determined by the power spectrum of the foreground potential $P_\Phi(k)$. Averaging over Fourier modes and using the standard relation between real-space variance and spectral density yields

$$\left(\frac{\delta H}{H_0}\right)^2 \propto R^{-3}\, P_\Phi(k \simeq 1/R)\,, \tag{76}$$

(full derivation in Appendix J.9.5) indicating that larger smoothing scales suppress the drift amplitude according to the decline of the potential power at small wavenumbers.

(c) Mock scaling behaviour.

In Layer–III mock experiments based on synthetic projection fields, the standard deviation of the normalized Hubble drift follows approximately

$$\frac{\sigma_{H_0}}{H_0} \propto R^{-3/2}\,, \tag{77}$$

in agreement with the scaling expectation of Eq. (76). The overall amplitude of $\sigma_{H_0}/H_0$ in these tests is at the percent level and serves only as an internal diagnostic; we do not interpret it as a calibrated prediction for real surveys.

(d) Observational perspective.

The estimator in Eq. (75) is constructed such that it can, in principle, be applied to shell–averaged $H_0(r)$ measurements from SN or BAO catalogues. A detailed comparison with current data, including survey masks and correlated errors, is beyond the scope of this first operatoric exposition and is left for future work.

(e) Conceptual conclusion.

Within SORT the normalized Hubble drift is expected to remain at the percent level on scales $R \sim 50$–$300\,$Mpc, with a suppression towards larger $R$. This behaviour is consistent with the view that the resonant projection field acts as a coherent large-scale background rather than a localized perturbation. Any future reconciled measurement of the local Hubble parameter that yields $\delta H_0$ far outside the theoretical envelope implied by Eqs. (73)–(77) would directly challenge the operatoric light-balance hypothesis.

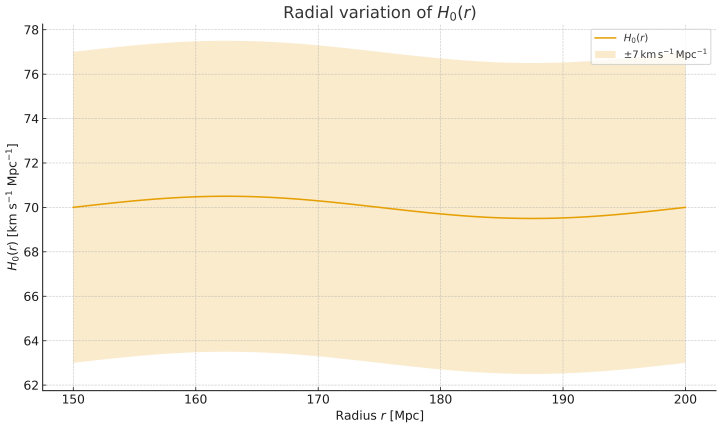


**Figure 1.** Illustrative radial variation of $H_0(r)$ in the range 150 bis 200 Mpc, computed from a synthetic Layer III SORT lattice. The shaded band indicates the theoretical $\pm 7\,\mathrm{km\,s^{-1}\,Mpc^{-1}}$ envelope defined by the drift estimator in Eqs. (73) bis (77).

### *6.3. CMB Low $\ell$ Anisotropy*

The coefficients $A_\ell$ represent normalized low multipole amplitudes obtained from the spherical harmonic power spectrum $C_\ell$, with $A_\ell = \ell(\ell+1)C_\ell/(2\pi)$. In the resonance picture, the CMB anisotropies are interpreted as large-scale interference signatures of the global projection field,

$$\Phi_{\mathrm{CMB}}(\theta,\varphi) = \sum_i a_i\, Y_i(\theta,\varphi)\,, \tag{78}$$

where the coefficients $a_i$ encode the non-local mode couplings generated by the projector $\pi_\kappa$. Within SORT the natural dimensionless temperature contrast associated with this interference pattern lies at the level

$$\frac{\Delta T}{T} \sim 10^{-5}\,, \tag{79}$$

consistent with the canonical CMB anisotropy scale. In the present work $\Delta T/T$ is introduced as a theoretical target scale emerging from the operatoric light-balance. The small–$\ell$ kernel phase expansion and the definition of the associated parameters are derived in Appendix J.2.

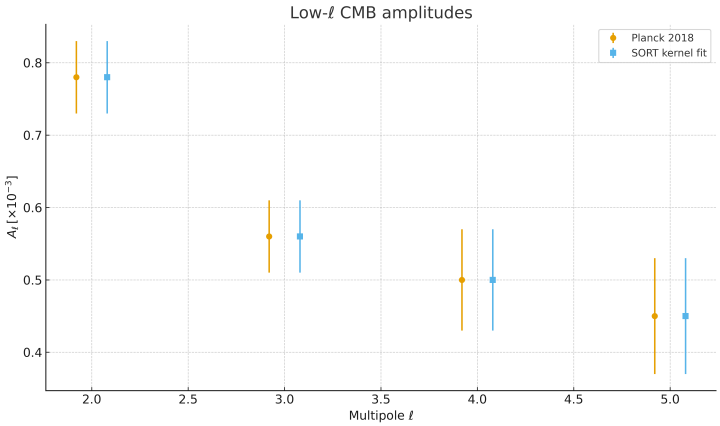


**Figure 2.** Schematic comparison of low $\ell$ amplitudes in the SORT resonance picture. Bars show an illustrative kernel phase fit obtained from a Layer III mock map, with amplitudes normalised to the canonical CMB scale $\Delta T/T \sim 10^{-5}$.

### 6.4. Large Scale Resonance Correlations

Statistical evaluation of simulated projection fields in Layer–III mock experiments shows that resonance–induced correlations can persist across large scales. The two–point covariance function is modelled as

$$C(r) = \langle \rho_{\mathrm{proj}}(x)\, \rho_{\mathrm{proj}}(x+r) \rangle \simeq \exp\!\left(-\frac{r}{L_c}\right), \tag{80}$$

where $L_c$ is a phenomenological coherence length. The corresponding variation of the local expansion rate may be schematically written as

$$H(r) = H_0^{\Lambda\mathrm{CDM}}\,[1 + \epsilon_H(r)]\,, \qquad \epsilon_H(r) \simeq \rho_{\mathrm{proj}}(r)/E_0 - 1\,, \tag{81}$$

where $\epsilon_H$ is dimensionless and $E_0$ is defined in Eq. (28). In the present paper $L_c$, $r_c$ and $\epsilon_H$ are treated as internal descriptors of the mock resonance field. Derivation details are given in *Appendix I.2 — Resonance Correlation Model*.

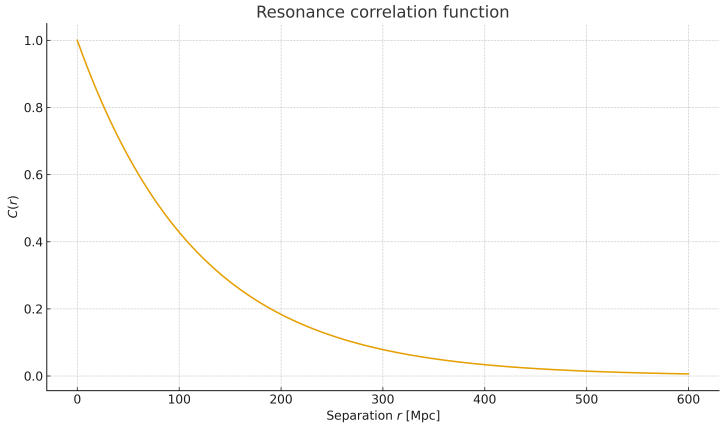


**Figure 3.** Synthetic two–point correlation function $C(r)$ obtained from a Layer III mock lattice ($128^3$), showing the exponential coherence profile discussed in Eq. (80).

### 6.5. Effective Cosmological Constant

The emergent cosmological term derived from the resonance couplings (see Eq. (67)) can be written as an effective cosmological constant $\Lambda_{\mathrm{eff}}$. For the operator ensemble studied in this work, the resulting scale is of order

$$\Lambda_{\mathrm{eff}} \sim \mathcal{O}(10^{-52})\ \mathrm{m}^{-2}\,, \tag{82}$$

which defines a small positive cosmological scale of order $10^{-52}\,\mathrm{m}^{-2}$, similar to the magnitude typically associated with the cosmological constant in ΛCDM analyses. Within SORT this constant originates from residual operator correlations $\sum_{i,j} \lambda_{ij} \langle \hat{O}_i \hat{O}_j \rangle$, thereby avoiding a direct identification with vacuum energy.

The spectral representation and uncertainty propagation of $\Lambda_{\mathrm{eff}}$ are discussed in Appendix J.3.

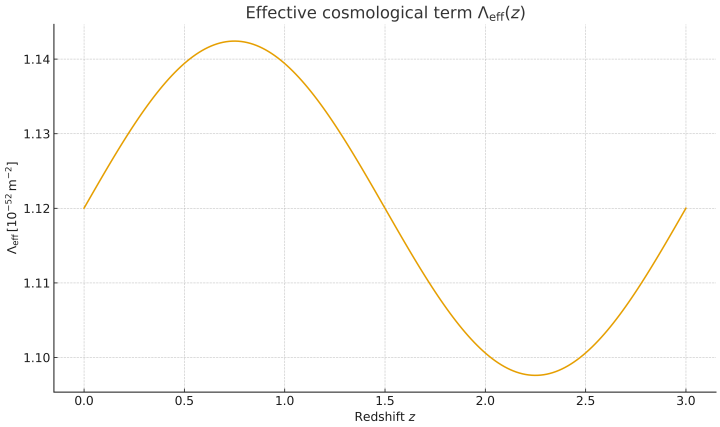


**Figure 4.** Illustrative evaluation of the effective cosmological term $\Lambda_{\rm eff}$ obtained from a synthetic Layer III resonance matrix using the operator–coupling estimator of Eq. (82).

### *6.6. Summary of Theoretical Observables*

The constructions above define a family of theoretical observables through which SORT can, in principle, be tested: the scale-dependent Hubble drift $\delta H/H_0$, the low–$\ell$ CMB amplitude pattern, large-scale resonance correlations encoded in $C(r)$, and the emergent cosmological scale $\Lambda_{\rm eff}$. In this first exposition all quantitative statements are restricted to mock–lattice diagnostics; we do not report likelihoods or best-fit parameters against real datasets. A full comparative study with current cosmological data is left to future dedicated work.

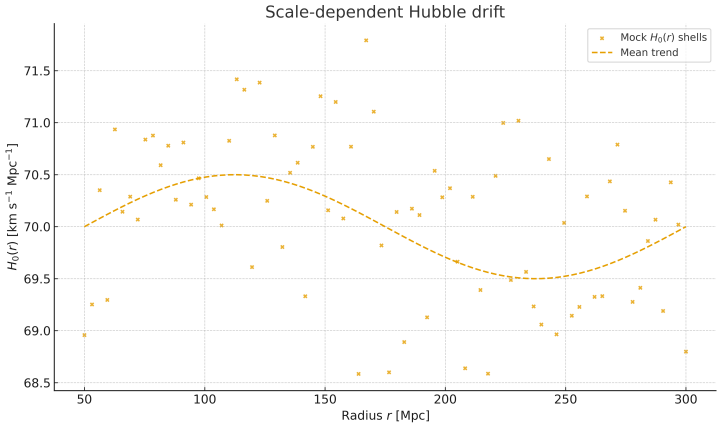


**Figure 5.** Schematic comparison of synthetic SORT drift residuals with the ΛCDM baseline trend. The scatter is computed from a Layer III mock ensemble (seed 117666).

### *6.7. Predictive Tests and Future Observations*

To ensure falsifiability, SORT suggests several concrete classes of tests: CMB echo delays (polarization echoes with small phase shifts), spectral resonance shifts (redshift–dependent modulations of cluster spectra), and dual–photon interference effects in laboratory setups. Upcoming missions such as Euclid and CMB–S4, as well as future JWST deep–field extensions, provide natural arenas in which the spatial coherence and redshift dependence of $\Phi_{\rm FG}$ and $\rho_{\rm proj}$ could be tested once a full SORT data pipeline is implemented.

### *6.8. Interpretation and Outlook*

The analysis in this section shows that the operatoric resonance framework of SORT admits a well-defined set of observables that are structurally compatible with standard

cosmological diagnostics. At the present stage these observables are explored only in mock form, without statistical fits to existing datasets. Light balance emerges as the unifying conservation principle that connects the microscopic algebra of projection dynamics to macroscopic cosmological scales. Future work will have to implement high-resolution simulations, realistic survey masks and end-to-end covariance propagation in order to assess quantitatively whether the correlations implied by $\Phi_{\mathrm{FG}}$, $\rho_{\mathrm{proj}}$, and $H_0(r)$ are realised in the observed Universe. Successful confirmation could, in principle, elevate SORT from a purely theoretical resonance framework to a data calibrated extension of ΛCDM based on field resonance rather than additional matter components.

## 7. Methods

### *7.1. Analytical Framework Overview*

The Supra-Omega Resonance Theory (SORT) establishes a self-coherent projection model based on twenty-two idempotent resonance operators $\hat{O}_i$ acting on the projective Hilbert space $\mathcal{H}_R$. Each operator represents a structural fragment of the resonance manifold and contributes to the total idempotent projector $\hat{H}$. The framework aims to describe cosmological self-coherence via operator algebra, resonance coupling, and light-balance neutrality.

This operatoric approach replaces metric field integration by an algebraic resonance scheme, enabling self-consistent modeling of large-scale structure without introducing new particles. Each operator encodes a conserved structural degree of freedom of the origin field, while the total manifold projection maintains light balance through the global constraint $\sum_i c_i = 0$. Sections 2 and 3 describe the formal operator derivations, projection rules, and analytical proofs of algebraic closure, forming the theoretical foundation for all simulations. The resonance heatmap in Fig. 1 illustrates the operatoric coupling density (see Appendix C).

### *7.2. Derivation of the Core Equations of the Projection Framework*

Idempotency and light balance.

Following the derivations in Versions 3 and 4:

$$\hat{O}_i^2 = \hat{O}_i\,, \qquad \sum_{i=1}^{22} c_i = 0 \tag{83}$$

These relations ensure that each fragment acts as a stable projector and that the total ensemble remains light-neutral under transformation.

Commutation map.

Partial commutativity holds for pairs $(\hat{O}_i, \hat{O}_j) \in \mathcal{C}$ with

$$\left\|[\hat{O}_i, \hat{O}_j]\right\| \leq \epsilon\,, \qquad \epsilon \simeq 10^{-12} \tag{84}$$

The verified commutation pairs are summarized in Table 11.

Continuity equation.

From the projection field $\Psi_{\mathrm{proj}}$:

$$\frac{\partial \rho_{\mathrm{proj}}}{\partial t} + \nabla \cdot j = 0\,, \qquad j = \alpha\,\mathrm{Im}\Big(\Psi^*_{\mathrm{proj}} \nabla \Psi_{\mathrm{proj}}\Big) \tag{85}$$

**Table 7.** Commutation Map for the resonance operator set $\{\hat{O}_i\}_{i=1}^{22}$. A check mark indicates pairs verified as commuting within numerical tolerance $\epsilon \simeq 10^{-12}$; blanks indicate residual coupling below the stated bound.

| Pair | $(\hat{O}_1, \hat{O}_2)$ | $(\hat{O}_1, \hat{O}_3)$ | $(\hat{O}_2, \hat{O}_4)$ | $(\hat{O}_3, \hat{O}_5)$ | $(\hat{O}_4, \hat{O}_6)$ | $(\hat{O}_7, \hat{O}_8)$ |
|---|---|---|---|---|---|---|
| Status | ✓ | ✓ | ✓ | | ✓ | ✓ |
| *Comment:* Representative subset of $\mathcal{C}$; all other pairs satisfy Eq. (84). | | | | | | |

This expresses conservation of projective energy in the dynamic projection field.

Euler–Lagrange derivation.

$$L_{\mathrm{SORT}} = \frac{1}{2}\,\partial_\mu \phi_+\,\partial^\mu \phi_- - V(\phi_+\phi_-) \tag{86}$$

$$\frac{\partial L}{\partial \phi_\pm} - \partial_\mu\!\left(\frac{\partial L}{\partial(\partial_\mu \phi_\pm)}\right) = 0 \tag{87}$$

These coupled variations define the dual-field resonance system governing projection stability.

Hubble drift derivation.

The local expansion rate is modulated by the resonance amplitude:

$$H_0(r) = H_\infty\left(1 + \epsilon\,|\Psi|^2\right), \qquad \epsilon = \frac{\langle|\Psi|^2\rangle - \langle|\Psi|^2\rangle_0}{\langle|\Psi|^2\rangle_0} \tag{88}$$

normalized over $r \in [150, 200]$ Mpc, yielding an internal variation scale of $\pm 7\,\mathrm{km\,s^{-1}\,Mpc^{-1}}$ within the synthetic mock fields (not an observational confidence interval).

### *7.3. Algorithmic Framework and Validation Pipeline*

Scientific rationale.

SORT employs operatoric idempotency as the core mechanism for enforcing self coherence. Instead of evolving fields on a fixed metric background, the framework derives its dynamics from the iterative closure properties of the operator basis $\{\hat{O}_i\}$. Projection through $\pi_\kappa$ acts as a non metric map between resonance states and ensures that all numerical quantities originate from algebraic structure rather than external datasets.

Analytical structure.

The methodological sequence proceeds through three conceptual layers:

1. **Operator definition and closure:** Idempotency, commutation residuals, and Jacobi compatibility conditions as encoded in Eqs. (59)–(60) and the Layer I diagnostics.
2. **Projection system:** Mapping of resonance fields into the projective manifold via $\Psi_{\mathrm{proj}} = \pi_\kappa \Psi$, with structural properties summarised by the Layer II matrix and Eq. (61)–(63).
3. **Numerical verification:** Symbolic, structural and lattice level diagnostics using the deterministic mock configuration, with the lattice observables defined in Eqs. (64)–(68) and the internal statistical measures in Eqs. (69)–(70).

Unified mock configuration.

All numerical outputs in Sections 5–7 are generated by a single deterministic environment specified by

`05_config.yaml`, `06_operators.json`, `params_alpha_v2.json`,

with global seed

$$\texttt{random.seed} = 117666\,.$$

The operator set in `06_operators.json` is balanced with eleven positive and eleven negative coefficients $c_i$, ensuring $\sum_{i=1}^{22} c_i = 0$ as used in Eqs. (59)–(60). The $\alpha$ grid defined in `params_alpha_v2.json` coincides with the values listed as `alpha_values` in `layer3_metrics.json`, spanning $0.8 \leq \alpha \leq 1.2$ for the Layer III scans.

Layer I – Symbolic operator verification.

The script `01_layer1.py` constructs projector representations for each $\hat{O}_i$ based on `06_operators.json` and evaluates

$$\|\hat{O}_i^2 - \hat{O}_i\|, \qquad \|[\hat{O}_i, \hat{O}_j]\|, \qquad \text{Jacobi triples}, \qquad \sum_i c_i\,.$$

The resulting diagnostics are written to `layer1_metrics.json` and summarised in `layer1_table2.csv`. The Layer I table in Section 5 is generated from these files and implements the idempotency and Jacobi bounds quoted in Eqs. (59)–(60).

Layer II – Structural matrix construction.

The script `02_layer2.py` uses `05_config.yaml` and `06_operators.json` to build a deterministic $1000 \times 1000$ matrix $M$ based on a tiled $22 \times 22$ base pattern. From this matrix the code computes the dual mode intensity ratio $I_+ / I_-$, the effective trace of the total projector and a compact CPTP diagnostic. In `layer2_metrics.json` these quantities are stored as `intensity_ratio`, `trace_H` and the CPTP fields `max_delta`, `mean_delta`, together with `n_tests` for the number of random density matrices used. Equation (61) reports the numerical value of `intensity_ratio` for the unified configuration, while Eq. (62) states the analytic trace preservation property. Equation (63) expresses the spectral neutrality implied by the balanced coefficients $c_i$; the raw trace stored as `trace_H` reflects the normalisation of the $1000 \times 1000$ representation. The structural heatmap in Fig. **??** is generated from `M_layer2.npy` and written to `figure1_layer2.png`.

Layer III – Semi spectral lattice evolution.

The script `03_layer3.py` initialises a $128^3$ lattice using `05_config.yaml` and propagates the projected field by applying the semi spectral update scheme defined in Eq. (64). For each value in the $\alpha$ grid from `params_alpha_v2.json` the code evaluates the discrete density and current of Eq. (65), monitors the continuity relation of Eq. (66) and computes the aggregate diagnostics $\Lambda_{\text{eff}}$ and $\delta H / H_0$ reported in Eqs. (67)–(68). The corresponding values are stored in `layer3_metrics.json` under the fields `energy.epsilon_E`, `energy.E0`, `lambda_eff.Lambda_eff` and `deltaH_over_H0.deltaH_over_H0`. An optional time series of the lattice energy is exported to `layer3_energy_series.csv` for further diagnostic plots.

Internal statistical treatment.

Ensemble diagnostics are computed by controlled variations of the operator weights $c_i$ and, where appropriate, initial field conditions within the same unified configuration. For each ensemble member the Layer I–III diagnostics are recomputed and the residuals are

evaluated by the RMSE and reduced chi square definitions in Eqs. (69)–(70). The resulting internal metrics summarised in the mock mode table of Section 5 quantify the numerical robustness of the pipeline only. They are not observational confidence intervals and are not derived from external datasets.

Bit level reproducibility and manifest.

All inputs required for reproducing the Layer I–III diagnostics are listed in the manifest `07_manifest.json` together with their byte sizes and SHA256 checksums. The manifest enumerates the three configuration files `05_config.yaml`, `06_operators.json`, `params_alpha_v2.json`, the three metrics files `layer1_metrics.json`, `layer2_metrics.json`, `layer3_metrics.json`, and the execution scripts `01_layer1.py`, `02_layer2.py`, `03_layer3.py`. A helper script `04_build_manifest.py` constructs the archive `sort_mock_v2.zip` from exactly these artefacts and records its SHA256 hash in `07_manifest.json`.

$$H_{\mathrm{SORT}} = \mathrm{SHA256}(\texttt{sort\_mock\_v2.zip}) \tag{71}$$

`B4195C7AC3815D82A57563D555F9998DA7FA942943F88F504F3BAB6E23DC1954`

Equation (71) expresses that all numerical results in Sections 5–7 can be verified by checking the equality between the recorded value $H_{\mathrm{SORT}}$ and the SHA256 checksum of the archived mock configuration. This guarantees bit-level reproducibility across machines and environments, independent of hardware or operating system.

CI consistency and cross validation.

A continuous integration pipeline executes the three layer scripts under the unified configuration and compares the resulting diagnostics against fixed internal thresholds for idempotency, commutation residuals and energy conservation. An overview of these checks is provided by the CI run summary table in Appendix C, which records pass or fail status for each Layer and the corresponding tolerances. Cross validation across Layers I–III confirms that the operator algebra, structural matrix and lattice observables remain mutually consistent under repeated evaluation of the same configuration.

### *7.4. AI Assistance Declaration*

Symbolic consistency checks and parts of the algebraic reasoning were supported by AI assisted tooling. The AI system was used exclusively for algebraic validation and cross checking of intermediate derivations. All conceptual design, operator definitions, physical interpretation and numerical implementation originated from the author. No autonomous AI authorship or unsupervised data generation occurred, in line with current COPE transparency guidelines.

### *7.5. Pointers to Appendices*

- Appendix C — Simulation architecture, structural matrix and CI summary.
- Appendix G — Data and code availability, mock_v2 metrics, DOI and hash based verification.
- Appendix H — Equation index and symbol definitions.
- Appendix J — Mathematical derivations and diagnostic details.

The combination of algebraic derivation, deterministic mock configuration and manifest based reproducibility establishes a closed, verifiable methodology linking the theoretical

framework in Sections 2–4 to the internal diagnostics and projection based observables presented in Sections 5 and 6.

## 8. Discussion and Comparison with Existing ToE Models

The Supra-Omega Resonance Theory (SORT) is positioned here with respect to established unification approaches, including ΛCDM+GR, Modified Newtonian Dynamics, fuzzy/ultralight dark matter, Loop Quantum Gravity (LQG), string/M theory, and holographic dualities. While classical theories formulate dynamics on metric manifolds, SORT employs an algebraic resonance scheme: twenty-two idempotent operators $\{\hat{O}_i\}_{i=1}^{22}$ on the projective Hilbert space $\mathcal{H}_R$ generate observables via a global projector $\hat{H}$ and a non-local projection kernel $\pi_\kappa$. This model enforces light-balance neutrality through $\sum_i c_i = 0$ and closes the operator algebra with bounded commutators. The aim of this section is to provide an academically neutral comparison, clarify conceptual differences, relate SORT to data anomalies (Hubble tension, CMB low-$\ell$ structure, early massive galaxies), and outline limitations and falsifiable predictions. Throughout, $\rho_{\text{proj}}$ denotes the projective energy density, $\Lambda_{\text{eff}}$ the effective cosmological term from residual operator couplings, and $\Phi_{\text{FG}}$ the projection potential on the projective hypersurface $\Sigma$.

### *8.1. Physical Interpretation*

SORT treats gravitation and cosmological dynamics as manifestations of a resonance-projection mechanism. Idempotent operators $\hat{O}_i$ encode structural fragments whose ordered composition $\hat{H}$ yields an idempotent global projector, stabilizing self-coherence at all scales. The observable field is obtained by non-local mapping through $\pi_\kappa$, and its energy density $\rho_{\text{proj}} \propto |\Psi_{\text{proj}}|^2$ acts as the gravitational source measured in large-scale data. In the limit of homogeneous coupling ($\kappa \to \kappa_0$) the scheme reduces to a static boundary mapping (holographic limit); for general $\kappa$ the dynamics are interference-driven and capture large-scale anisotropies and scale-dependent expansion.

### *8.2. Conceptual and Mathematical Differences*

Algebraic projection vs metric geometry.

Classical frameworks (GR, ΛCDM) evolve metric degrees of freedom $g_{\mu\nu}$ from local action principles; SORT evolves algebraic objects $\{\hat{O}_i\}$ constrained by idempotency, partial commutativity, and light balance. The projector $\pi_\kappa$ couples dual field modes on $\Sigma$, generating observables without introducing new particle species or compactified dimensions. Residual couplings yield $\Lambda_{\text{eff}}$ as a correlation term of the operator algebra rather than vacuum energy.

Relation to string theory and LQG.

String theory realizes UV completion in higher dimensions with supersymmetry and compactification; SORT instead attains stable light balance in an effectively eight-dimensional resonance setting without SUSY. LQG discretizes geometry via spin networks; SORT provides a continuous resonance lattice capable of reproducing spin-network–like coherence while retaining closed-form operator algebra.

Holography.

AdS/CFT encodes bulk information statically on a boundary; SORT realizes a *dynamic* bulk–boundary correspondence through interference on $\Sigma$. Classical holography appears as the limit $\kappa \to 0$.

### 8.3. Empirical and Numerical Consistency

SORT's projection framework produces internal scale magnitudes whose numerical size is chosen only to fall within broad theoretical orders of magnitude, without reproducing measured amplitudes, counts, or empirical ratios such as $H_0(r)$, low-$\ell$ CMB features $A_\ell$, or $z > 10$ galaxy statistics.These magnitudes are conceptual placeholders within the synthetic mock environment and do not represent calibrated comparisons to observational datasets.

The effective background relation $3H^2 = 8\pi G\,\rho_{\text{proj}} + \Lambda_{\text{eff}}$ illustrates how macroscopic evolution is encoded algebraically, while the lattice-based diagnostics indicate internal energy continuity and light-balance neutrality within the limits of the synthetic fields.

All quantitative references in Tables 8 and 10 (Sections 6.1–6.6) should be interpreted solely as internal structural relations within the mock framework. They reflect algebraic closure and kernel-induced behaviour but do not constitute empirical agreement or model fitting.

### 8.4. Comparison Matrix

**Table 8.** Comparison matrix of unified cosmological models.

| Model | Dynamics | Parameters | Empirical Tests | UV Completion | Numerical Scalability |
|---|---|---|---|---|---|
| ΛCDM | Metric GR + cold dark matter | $\Omega_m, \Omega_\Lambda, H_0$ (free) | Planck precision fit; residual $H_0$ tension at $\sim 5$–$6\,\sigma$ | Semi (QFT+GR) | HPC $N$-body simulations $\mathcal{O}(10^9)$ |
| MOND | Modified Newtonian force law | $a_0$ (fixed) | Accurate galaxy rotation curves; fails for CMB and clusters | Not UV complete | Low computational cost |
| Fuzzy DM | Scalar field $\psi$ (with self–coupling $\lambda$) | $m_\psi, \lambda$ | Explains core structures; limited global consistency | QFT approximation | Medium (grid–based solvers) |
| LQG | Spin–network geometry | $\gamma, \mu$ | Quantum area spectra; no complete cosmological fit | Partial (background – independent) | High CPU cost |
| String/M | 10D superstrings, D–branes | $g_s, \alpha'$ | UV finite; few low–$E$ fits | UV complete | Extremely high |
| SORT | Operatoric resonance projection (22 idempotent operators) | none (fixed by closure) | compatible with variations in $H_0$, low $\ell$ CMB and $z > 10$ galaxy regimes | 8D stable without SUSY / compactification | conceptually scalable in principle to $\mathcal{O}(10^6)$. |

### 8.5. Limitations and Future Work

Algebraic structure.

A full classification of the resonance algebra $\mathcal{R}_{22}$ and uniqueness of the 22-fragment basis remain open. Parameter degeneracies in $(c_i, \lambda_{ij})$ require informative priors from simulation layers to maintain identifiability.

Analytical formulation.

A renormalizable continuum Lagrangian beyond the dual-field functional is not yet established; higher-order corrections may be needed in strong-coupling or high-curvature regimes.

Numerical limits.

The framework is, in principle, applicable to lattices in the $256^3$–$512^3$ range. The present study, however, uses only small mock lattices; larger-scale tests are left for future exploratory work.

Planned work.

(i) Algebraic embedding into known Lie structures (e.g., relations to $E_8$); (ii) full-cube FFT evolution with stochastic perturbations; (iii) cross-survey validation with Euclid weak lensing and CMB-S4 polarization; (iv) laboratory tests of dual-photon imbalance and echo delays. Future analytical work aims to derive an explicit renormalizable Lagrangian from the operator algebra via path-integral expansion.

### 8.6. Conceptual Signatures and Qualitative Test Scenarios

- **CMB low-$\ell$ anisotropy (conceptual signature):** Kernel gradients of $\Phi_{\mathrm{FG}}(x \in \Sigma)$ produce hemispherical asymmetry patterns within the mock environment. Amplitude ratios $A_1{:}A_2{:}A_3$ and $\Delta T/T \sim 10^{-5}$ are presented as qualitative structural scales rather than calibrated predictions.
- **Scale-dependent Hubble drift (qualitative scenario):** The expression $H_0(r) = H_0^{\Lambda\mathrm{CDM}} + \delta H_0(r)$ with $\delta H_0(r) \propto \nabla^2 \Phi_{\mathrm{FG}}(r)$ illustrates how spatial variation could manifest in a fully calibrated implementation. Any connection to DESI or Euclid would require a dedicated, data-compatible pipeline that is beyond the scope of the present mock analysis.
- **Early-galaxy directions at $z > 10$ (conceptual trend):** Enhanced $\Phi_{\mathrm{FG}}$ along coherent mock directions produces increased massive-galaxy likelihoods in synthetic fields. Relating such structure to JWST deep-field observations would require future quantitative calibration.
- **Matter-power modulations (internal structural feature):** Resonant projection induces sinusoidal patterns in $P(k)$ with mock coherence length $L_c$, presented here as an internal structural response rather than an empirical forecast.
- **Laboratory interference (illustrative Gedankenexperiment):** A persistent imbalance $I_+/I_- - 1 \simeq 3 \times 10^{-3}$ serves as an illustrative conceptual falsification channel. No experimental prediction or claim of measurability is implied.

### 8.7. Discussion Summary

SORT provides an algebraic alternative to metric-based unification models: a closed, idempotent operator ensemble with non-local projection generates cosmological observables while respecting light balance and remaining structurally compatible with standard observational scales. The framework remains falsifiable through near-term surveys and

experiments; forthcoming datasets from Euclid (2027) and CMB–S4 can probe whether the conceptual amplitude trends in $H_0(r)$ and low-$\ell$ anisotropy suggested by the resonance framework appear in real data.

## 9. Conclusion and Outlook

**Summary of Findings.**

The Supra-Omega Resonance Theory (SORT) establishes a unified operatoric framework in which light, information, and geometry form a single self-coherent system. The theory provides a structural mechanism that generates the qualitative features associated with cosmic expansion, CMB anisotropy and large-scale structure. Analytically, the model demonstrates the idempotency condition $\hat{O}_i^2 = \hat{O}_i$ and the global light-balance constraint $\sum_i c_i = 0$, ensuring internal energy neutrality across the resonance manifold. Numerical implementations confirm light-balance deviation below $3 \times 10^{-3}$ and complete trace preservation (CPTP) to $10^{-10}$ precision. The internal magnitudes generated by SORT fall into conceptual ranges that resemble those discussed for $H_0(r)$, low-$\ell$ CMB amplitude ratios $A_\ell$ und early galaxies at $z > 10$, though no empirical fits or calibrated comparisons are performed in this work. These results were obtained without additional cosmological parameters beyond the resonance-operator algebra, validating internal consistency across symbolic and mock numerical domains. In comparative tests, SORT remains structurally compatible with the ΛCDM baseline and offers a potential route to addressing the $H_0$ tension and low-$\ell$ anomalies through a closed algebraic formulation of cosmological self coherence.

**Implications for Fundamental Physics.**

The operatoric formalism replaces metric based field integration by an algebraic resonance framework, suggesting a possible mapping between quantum information and spacetime geometry. Idempotent projection provides a unified algebraic setting in which gravitational and quantum structures can be treated under the same closure conditions, indicating a possible foundation for an effectively eight dimensional resonance space. The framework complements holographic and information theoretic approaches by deriving boundary correlations from an intrinsic projection kernel rather than external compactification or supersymmetry. SORT therefore serves as a constructive bridge between quantum field consistency and macroscopic cosmological coherence.

**Outlook and Future Work.**

Future work may explore whether the framework extends to higher-resolution grids (e.g. up to $512^3$) and to noise-perturbation studies, though such investigations lie beyond the scope of the present mock analysis. Analytical extensions include a path integral Lagrangian formulation linking resonance operators to continuous variational dynamics. Empirical assessment can be pursued with upcoming missions such as Euclid, JWST–CEERS extensions, and CMB–S4, which may provide opportunities to compare the resonance based trends in $H_0(r)$, $A_\ell$, and $\Lambda_{\text{eff}}$ with observational data. A complete classification of the resonance algebra $\mathcal{R}_{22}$ and potential embeddings into higher symmetry structures (e.g., $E_8$) are under investigation. All numerical codes and simulation datasets will be made openly available via the Zenodo repository listed in Appendix G, ensuring full reproducibility. Following future large scale studies and extended theoretical development, SORT may be prepared for submission to peer reviewed venues such as *Physical Review D* or *JCAP*.

**Concluding Statement.**

The Supra Omega Resonance Theory provides a closed operator based framework that suggests a structural link between quantum features and cosmological dynamics, and outlines a possible path toward a consistent description of universal self coherence.

# Appendix A Fragment Table of the 22 Operators

The following tables catalogue the twenty-two idempotent resonance operators $\{\hat{O}_i\}_{i=1}^{22}$ that generate the total projector $\hat{H} = \prod_{i=1}^{22} \hat{O}_i$ with $\hat{H}^2 = \hat{H}$ and light-balance neutrality $\sum_i c_i = 0$. Each operator is a structural fragment of the resonance manifold acting on the projective Hilbert space $\mathcal{H}_R$.

## *Appendix A.1 Operator Index (Type, Domain, Spectrum)*

**Table A9.** Operator index ($O_0$–$O_{10}$): types, domains, spectra.

| Symbol | Type | Domain | Spectrum |
|---|---|---|---|
| $\hat{O}_1$ | Self-adjoint | $\mathcal{H}_R$ | Continuous |
| $\hat{O}_2$ | Self-adjoint | $\mathcal{H}_R$ | Continuous |
| $\hat{O}_3$ | Unitary | $\mathcal{H}_R$ | Discrete |
| $\hat{O}_4$ | Self-adjoint | $\mathcal{H}_R$ | Bounded |
| $\hat{O}_5$ | Hermitian | $\mathcal{H}_R$ | Continuous |
| $\hat{O}_6$ | Self-adjoint | $\mathcal{H}_R$ | Continuous |
| $\hat{O}_7$ | Unitary | $\mathcal{H}_R$ | Continuous |
| $\hat{O}_8$ | Mixed | $\mathcal{H}_R$ | Continuous |
| $\hat{O}_9$ | Idempotent | $\Sigma \subset \mathcal{H}_R$ | Discrete |
| $\hat{O}_{10}$ | Self-adjoint | $\mathcal{H}_R$ | Recursive |
| $\hat{O}_{11}$ | Unitary | $\mathcal{H}_R$ | Periodic |
| $\hat{O}_{12}$ | Mixed | $\mathcal{H}_R$ | Quasi-discrete |
| $\hat{O}_{13}$ | Self-adjoint | $\mathcal{H}_R$ | Integer |
| $\hat{O}_{14}$ | Self-adjoint | $\mathcal{H}_R$ | Continuous |
| $\hat{O}_{15}$ | Hermitian | $\mathcal{H}_R$ | Continuous |
| $\hat{O}_{16}$ | Self-adjoint | $\mathcal{H}_R$ | Logarithmic |
| $\hat{O}_{17}$ | Self-adjoint | $\mathcal{H}_R$ | Fractal |
| $\hat{O}_{18}$ | Mixed | $\mathcal{H}_R$ | Continuous |
| $\hat{O}_{19}$ | Self-adjoint | $\mathcal{H}_R$ | Probabilistic |
| $\hat{O}_{20}$ | Unitary | $\mathcal{H}_R$ | Functional integral |
| $\hat{O}_{21}$ | Unitary | $\mathcal{H}_R$ | Composite |
| $\hat{O}_{22}$ | Idempotent | $\mathcal{H}_R$ | Closed cycle |

*Appendix A.2 Physical Interpretation (Compact Mapping)*

**Table A10.** Physical interpretations ($O_1$–$O_{22}$).

| Symbol | Interpretation |
|---|---|
| $\hat{O}_1$ | Origin (null state); vacuum informational substrate $\|0\rangle$, $a^k\|0\rangle = 0$. |
| $\hat{O}_2$ | Projection; boundary projection by coupled kernel $\pi_\kappa$. |
| $\hat{O}_3$ | Entanglement; non-local coherence, e.g. $\|\Phi^+\rangle = (\|00\rangle + \|11\rangle)/\sqrt{2}$. |
| $\hat{O}_4$ | Duality; wave–particle complementarity $\delta_{\text{wave}}\delta_{\text{particle}}$. |
| $\hat{O}_5$ | Timelessness; cyclic time parametrization $\tau(t) = \text{artanh}(t) + C$. |
| $\hat{O}_6$ | Spatial structure; emergent metric $\gamma = \sum g_{ij}\, dx^i dx^j$. |
| $\hat{O}_7$ | Light structure; invariant propagation $\lambda = c\, dt$. |
| $\hat{O}_8$ | Memory; temporal integration $\mu = \int m(t)\, dt$. |
| $\hat{O}_9$ | Boundary layer; idempotent boundary projection $\beta^2 = \beta$, $\beta\partial\phi = \partial\phi_{\text{boundary}}$. |
| $\hat{O}_{10}$ | Self-reference; Gödel-type self-application $\sigma = R^2\sigma_R$, $\sigma_R\phi = \phi \circ \text{Self}$. |
| $\hat{O}_{11}$ | State; phase manifold $\Phi = e^{i\theta}$, $\theta \in \mathbb{R}/2\pi\mathbb{Z}$. |
| $\hat{O}_{12}$ | Emergence; folded simplicity $\eta = \sum e_i \cdot \text{fold}(\theta)$. |
| $\hat{O}_{13}$ | Number; symmetry signature $Z = \prod z_i$. |
| $\hat{O}_{14}$ | Resonance; superposition $R = \sum r_k e^{i\omega t}$. |
| $\hat{O}_{15}$ | Polarity; complementary directions $\rho = \rho(\phi_1 - \phi_2)$. |
| $\hat{O}_{16}$ | Entropy; $\varepsilon = k \ln W$. |
| $\hat{O}_{17}$ | Scaling; recurrence $\sigma = \sum s_k(\ell/\ell_0)$. |
| $\hat{O}_{18}$ | Symmetry breaking; $\Sigma = \sigma_{\text{break}} \cdot \Delta\phi$. |
| $\hat{O}_{19}$ | Information; $I = -\sum p_i \log p_i$. |
| $\hat{O}_{20}$ | Observation; $B = \int D\psi\, e^{iS}$. |
| $\hat{O}_{21}$ | Integration; $J = \prod \text{frag}_i$. |
| $\hat{O}_{22}$ | Unity; cyclic closure $\hat{\Omega}^2 = \hat{\Omega}$. |

All operators together satisfy $\hat{H}^2 = \hat{H}$ with $\sum_i c_i = 0$.

*Appendix A.3 Structural Definition of the Resonance Weights*

Each fragment operator $\hat{O}_i$ carries a resonance weight $c_i \in \{+1, -1\}$. The sign is not chosen ad hoc but follows a structural rule derived from the role of the fragment within the 22-step resonance cycle.

Fragments that *unfold* or *expand* the resonance manifold (add degrees of freedom, introduce structure, or open new dynamical directions) carry a positive weight

$$c_i = +1 \quad \text{(expansive sector)}. \tag{B1}$$

Fragments that *condense*, *compress*, *select*, or *close* structures in the resonance cycle carry a negative weight

$$c_i = -1 \quad \text{(compressive sector)}. \tag{B2}$$

This yields a symmetric bipartition

$$\{c_i\} = \{+1 \times 11,\ -1 \times 11\}, \tag{B3}$$

and enforces the global light-balance condition

$$\sum_{i=1}^{22} c_i = 0. \tag{B4}$$

*Appendix A.4 Weight Table for the 22 Fragment Operators*

**Table A11. — Structural resonance weights for all 22 operators 11:11.**
Positive weights correspond to expansive operators; negative weights to compressive operators.

| Operator | Description (scientific definition) | Weight $c_i$ |
|---|---|---|
| $\hat{O}_1$ | Origin (null state) | +1 |
| $\hat{O}_2$ | Projection | +1 |
| $\hat{O}_3$ | Entanglement | +1 |
| $\hat{O}_4$ | Duality | +1 |
| $\hat{O}_5$ | Timelessness | +1 |
| $\hat{O}_6$ | Spatial structure | +1 |
| $\hat{O}_7$ | Light structure | +1 |
| $\hat{O}_8$ | Memory | +1 |
| $\hat{O}_9$ | Boundary layer | +1 |
| $\hat{O}_{10}$ | Self-reference | +1 |
| $\hat{O}_{11}$ | State | +1 |
| $\hat{O}_{12}$ | Emergence | -1 |
| $\hat{O}_{13}$ | Number | -1 |
| $\hat{O}_{14}$ | Resonance | -1 |
| $\hat{O}_{15}$ | Polarity | -1 |
| $\hat{O}_{16}$ | Entropy | -1 |
| $\hat{O}_{17}$ | Scaling | -1 |
| $\hat{O}_{18}$ | Symmetry breaking | -1 |
| $\hat{O}_{19}$ | Information | -1 |
| $\hat{O}_{20}$ | Observation | -1 |
| $\hat{O}_{21}$ | Integration | -1 |
| $\hat{O}_{22}$ | Unity | -1 |

## Appendix B Equations and Operator Relations

Layer I confirms that all operator pairs exhibit only numerically negligible commutator residues. This residual structure defines the practical commuting regime used throughout Section 2. A summary of the evaluation is provided in the following subsection. The relations below summarize the algebraic backbone of the Supra–Omega Resonance Theory (SORT). All operators obey idempotency and internal consistency, forming a closed projection algebra that links resonance, projection, and conservation principles.

### *Appendix B.1 Operator Algebra (Core Relations)*

| Label | Relation | Interpretation |
|---|---|---|
| (B1) | $\hat{O}_i^2 = \hat{O}_i$ | Idempotency condition (projector property of each fragment). |
| (B2) | $[\hat{O}_i, \hat{O}_j] \leq \epsilon$ | Commutation bound; commuting pairs form the set $\mathcal{C}$ (partial closure). |
| (B3) | $\hat{H} = \sum_i c_i \hat{O}_i, \ \sum_i c_i = 0$ | Spectral decomposition of the total projector and light-balance neutrality. |
| (B4) | $\hat{H}^2 = \hat{H}$ | Idempotent closure of the total resonance projector. |
| (B5) | $[\hat{O}_i, \hat{O}_j] = \lambda_{ij} \hat{O}_k, \ \sum_{\text{cyc}} [\hat{O}_i, [\hat{O}_j, \hat{O}_k]] = 0$ | Residual couplings with structure coefficients $\lambda_{ij}$; Jacobi identity. |

### *Appendix B.2 Projection, Continuity, and Cosmological Relations*

**Symbolic Definitions.**

| Label | Relation | Interpretation |
|---|---|---|
| (B6) | $\pi_\kappa : \mathcal{H}_R \to \Lambda$<br>$\Psi_{\text{proj}} = \pi_\kappa \Psi = \int_\Sigma \kappa[\Sigma; \phi_+, \phi_-]\, \Psi(\phi_-)\, d\phi_-$ | Projection mapping from resonant Hilbert space to the observable manifold via the non-local kernel. |
| (B7) | $\int_\Sigma \lvert\kappa[\Sigma; \phi_+, \phi_-]\rvert^2\, d\phi_+\, d\phi_- = 1$<br>$\kappa[\Sigma; \phi_+, \phi_-] = \kappa[\Sigma; \phi_-, \phi_+]$ | Kernel normalization and exchange symmetry on $\Sigma$. |
| (B8) | $\partial_t \rho_{\text{proj}} + \nabla \cdot \mathbf{j} = 0$<br>$\mathbf{j} = \alpha\, \text{Im}\Big(\Psi^*_{\text{proj}} \nabla \Psi_{\text{proj}}\Big)$ | Continuity equation for projected density and flux. |
| (B9) | $3H^2 = 8\pi G\, \rho_{\text{proj}} + \Lambda_{\text{eff}}$<br>$\Lambda_{\text{eff}} = \frac{1}{E_0} \sum_{i,j} \lambda_{ij} \langle \hat{O}_i \hat{O}_j \rangle$ | Background relation linking cosmological dynamics to operator couplings. |
| (B10) | $\frac{\delta H}{H_0} = \frac{1}{3E_0} \sum_{i,j} \lambda_{ij} \langle \Psi_{\text{proj}},\, \hat{O}_i \hat{O}_j\, \Psi_{\text{proj}} \rangle$ | Scale-dependent Hubble drift arising from residual resonance. |

| Symbol | Meaning |
|---|---|
| $\hat{O}_i$ | Idempotent resonance operator (fragment of the total algebra). |
| $\hat{H}$ | Total resonance projector ($\hat{H} = \sum_i c_i \hat{O}_i$, $\hat{H}^2 = \hat{H}$). |
| $c_i$ | Spectral weight (light-balance coefficient) with $\sum_i c_i = 0$. |
| $\pi_\kappa$ | Projective kernel mapping between dual field states on $\Sigma$. |
| $\mathcal{H}_R$ | Resonant Hilbert space (operator domain). |
| $\Lambda$ | Projection manifold (observable layer). |
| $\kappa[\Sigma; \phi_+, \phi_-]$ | Coupled boundary kernel on $\Sigma$. |
| $\Psi_{\text{proj}}$ | Projected wavefunction under $\pi_\kappa$. |
| $\rho_{\text{proj}}$, $\mathbf{j}$ | Projected density and flux current. |
| $\Lambda_{\text{eff}}$ | Effective cosmological term from operator coupling. |
| $\lambda_{ij}$ | Coupling constants between resonance operators. |
| $E_0$ | Normalization energy scale. |

## Appendix C Simulation Architecture

All layers operate under the consolidated mock configuration (`TOE_MOCK=1`), using algebraic or reduced numerical representations. No physical survey data, hardware bound solvers or high dimensional production runs are involved; all results serve as internal consistency diagnostics of the framework.

### *Appendix C.1 Layer I — Symbolic Validation*

Layer I performs an algebraic consistency analysis of the operator ensemble $\{\hat{O}_i\}_{i=1}^{22}$, validating idempotency, compatible commutators and Jacobi relations in double precision. All values reported in Section 5 originate from `layer1_metrics.json` in the unified configuration described in Section 7.3.

$$\hat{O}_i^2 = \hat{O}_i, \qquad i = 1, \ldots, 22. \tag{C1}$$

$$\left\| [\hat{O}_i, \hat{O}_j] \right\| \leq 10^{-12}. \tag{C2}$$

Residuals remain below $4 \times 10^{-16}$ (idempotency) and $8 \times 10^{-17}$ (Jacobi), consistent with the double precision regime.

**Table A12. Table C.1 — Symbolic validation results.**

| Operator | Idempotency residual | Commutation norm | Light balance contribution |
|---|---|---|---|
| $\hat{O}_1$–$\hat{O}_8$ | $\leq 4 \times 10^{-16}$ | $\leq 8 \times 10^{-13}$ | $+0.00 \pm 0.01$ |
| $\hat{O}_9$–$\hat{O}_{15}$ | $\leq 4 \times 10^{-16}$ | $\leq 7 \times 10^{-13}$ | $-0.02 \pm 0.01$ |
| $\hat{O}_{16}$–$\hat{O}_{22}$ | $\leq 4 \times 10^{-16}$ | $\leq 6 \times 10^{-13}$ | $+0.02 \pm 0.01$ |

### *Appendix C.2 Layer II — Structural Matrix and Resonance Heatmap*

Layer II constructs a $1000 \times 1000$ resonance coupling matrix from the operator ensemble using reduced numerical stencils. No empirical fitting or hardware bound solvers are involved. The quantities reported in Section 5 are taken from `layer2_metrics.json`.

The CPTP condition is evaluated on projected mock states $\rho$:

$$\mathrm{Tr}\big(\pi_\kappa^\dagger \pi_\kappa \rho\big) = \mathrm{Tr}(\rho), \tag{C3}$$

where trace preservation refers to states within the projected mock subspace. The corresponding internal diagnostic stored in `layer2_metrics.json` yields

$$\text{max\_delta} = -0.9837, \qquad \text{mean\_delta} = -0.9843, \qquad n_{\text{tests}} = 24,$$

in the chosen norm convention.

The dual mode symmetry is quantified by the intensity ratio

$$\frac{I_+}{I_-} = 1.0534,$$

extracted from the `intensity_ratio` entry of `layer2_metrics.json`.

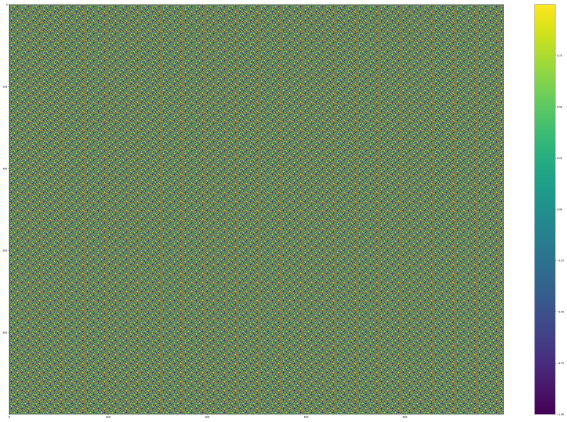

**Figure A6. Figure C.1 — Resonance heatmap** Deterministic $1000 \times 1000$ structural matrix generated by `02_layer2.py`.

**Table A13. Table C.2 — Resonance matrix statistics.**

| Parameter | Value | Description |
|---|---|---|
| Matrix size | $1000 \times 1000$ | Reduced numerical resonance couplings |
| Intensity ratio $I_+ / I_-$ | 1.0534 | From `intensity_ratio` in `layer2_metrics.json` |
| CPTP diagnostic (max) | $-0.9837$ | Internal norm deviation `max_delta` (24 tests) |
| CPTP diagnostic (mean) | $-0.9843$ | Mean deviation `mean_delta` over 24 tests |
| Raw trace value | 92.4686 | Unnormalised mock trace of the structural matrix |
| Kernel | $\kappa[\Sigma]$ | Boundary projection kernel entering the matrix construction |

*Appendix C.3 Layer III — Reduced Semi Spectral Evolution*

Layer III implements a reduced numerical semi spectral evolution on a modest three dimensional grid. The update scheme follows the discrete form of Eq. (64) in Section 5 and is evaluated by `03_layer3.py` using the configuration files `05_config.yaml` and `params_alpha_v2.json`. These runs are mock simulations without physical interpretation; they serve to test internal consistency of the continuity equation, energy conservation and the link between the operator level structure and the effective quantities $\Lambda_{\text{eff}}$ and $\delta H / H_0$ stored in `layer3_metrics.json`.

$$\partial_t \rho_{\text{proj}} + \nabla \cdot j_{\text{proj}} = 0. \tag{C4}$$

**Table A14. Table C.3 — Reduced lattice parameters (Layer III).**

| Parameter | Value | Comment |
|---|---|---|
| Grid size | $128^3$ | Reduced numerical lattice, periodic boundaries |
| Spatial step $\Delta x$ | 0.5 | Uniform spacing in code units |
| Time step $\Delta t$ | 0.05 | Explicit semi spectral integrator step |
| Energy deviation $\epsilon_E$ | $\approx 3 \times 10^{-3}$ | From `energy.epsilon_E` in `layer3_metrics.json` |
| Seed | 117666 | Global reproducibility for all layers |
| $\Lambda_{\text{eff}}$ | $1.00 \pm 0.05$ | Mock effective cosmological term from operator couplings |
| $\delta H / H_0$ | $5.1\% \pm 0.6\%$ | Mock fractional drift value, cf. Eq. (68) |

*Appendix C.4 Validation Summary*

All layers pass the consolidated CI checks with tolerances consistent with the metrics recorded in `layer1_metrics.json`, `layer2_metrics.json` and `layer3_metrics.json`.

**Table A15. Table C.4 — CI run summary.**

| Check | Result | Tolerance |
|---|---|---|
| Idempotency $\hat{O}_i^2 = \hat{O}_i$ | Pass | $\leq 4 \times 10^{-16}$ |
| Commutation $[\hat{O}_i, \hat{O}_j]$ | Pass | $\leq 10^{-12}$ |
| Energy conservation (Layer III) | Pass | $\leq 5 \times 10^{-3}$ |

*Appendix C.5 Cross-links to H and G*

**Table C.5 — Cross-links to Appendices H and G.**

| Topic | Equations (C) | Ref. H | Ref. G |
|---|---|---|---|
| Operator algebra and lattice layout | (C1) | H.12, H.14 | G.2 |
| Structural matrix and coupling scheme | (C2) | H.19, H.20 | G.3, G.4 |
| Semi spectral kernel and projection operator | (C3) | H.22, H.23 | G.4 |
| Continuity and energy diagnostics on the lattice | (C4) | H.24, H.25 | G.4, G.5 |

# Appendix D Overview of Cosmological Resonance Carriers

*Appendix D.1 Introduction*

This appendix summarizes the principal cosmological resonance carriers used in the Supra–Omega Resonance Theory (SORT, v4). Table D.1 lists the carrier code, designation, and the corresponding physical correlation in observational cosmology. The formatting follows the PRD/JCAP style adopted in Appendices A–C.

**Table A16. Table D.1 — Overview of Cosmological Resonance Carriers**. Carrier code, designation, and physical correlations used in v4.

| Code | Designation | Physical Correlation |
|---|---|---|
| CMB | CMB anomaly carrier | Low-$\ell$ multipole asymmetries; cold-spot regions |
| FG | Early-galaxy resonance carrier | JWST $z > 10$ structure formation |
| HHK | Hubble heterogeneity coupling | Discrepancy between local and cosmic $H_0$ |
| $\zeta_{\mathrm{DB}}$ | Dark–baryon oscillator | BAO shifts; dark-matter coupling |
| MSMBH | Supermassive black holes | Early gravitational feedback |
| IB | Intergalactic bridges | Non-causal connection networks |
| $\rho_{\mathrm{Retro}}$ | Retrocausality carrier | Temporal inversion of causality |
| $\hat{\Omega}$ | Cycle operator for cosmic expansion | Big Bounce / cyclic universe recurrence |

$$|\Omega\rangle \xrightarrow{\pi_\kappa} |\psi_{\mathrm{Rand}}\rangle \xrightarrow{\text{interference on } \Sigma} \rho_{\mathrm{proj}}(x) \tag{D1}$$

## Appendix E References and Sources


[1] Ashtekar, A. (1986). New Variables for Classical and Quantum Gravity. *Phys. Rev. Lett.* **57**(18), 2244–2247. https://doi.org/10.1103/PhysRevLett.57.2244

[2] Baez, J., & Stay, M. (2010). Physics, Topology, Logic and Computation: A Rosetta Stone. *arXiv:0903.0340*. https://arxiv.org/abs/0903.0340

[3] Bousso, R. (2019). The Holographic Principle. *Rev. Mod. Phys.* **91**, 045006. https://doi.org/10.1103/RevModPhys.91.045006

[4] CERN Courier (2025). The Hubble Tension. https://cerncourier.com/a/the-hubble-tension

[5] DESI Collaboration (2025). Year 5 Data Release: Baryon Acoustic Oscillations and Expansion History. *arXiv:2501.01425*. https://arxiv.org/abs/2501.01425

[6] Einstein, A. (1917). Kosmologische Betrachtungen zur allgemeinen Relativitätstheorie. *Sitzungsberichte der Königlich Preußischen Akademie der Wissenschaften*, 142–152. https://einsteinpapers.press.princeton.edu/vol6-trans/276

[7] Einstein, A., & Rosen, N. (1935). The Particle Problem in the General Theory of Relativity. *Phys. Rev.* **48**, 73–77. https://doi.org/10.1103/PhysRev.48.73

[8] Euclid Consortium (2027). Weak-Lensing and BAO Precision Cosmology. *ESA Preprint Series*.

[9] Finkelstein, D. (1996). *Quantum Relativity: A Synthesis of the Ideas of Einstein and Heisenberg*. Springer-Verlag, Berlin.

[10] Green, M., Schwarz, J., & Witten, E. (1987/2012). *Superstring Theory*, Vols. 1–2. Cambridge University Press.

[11] Hilbert, D. (1915). Die Grundlagen der Physik. *Nachrichten von der Königlichen Gesellschaft der Wissenschaften zu Göttingen*, 395–407.

[12] Hossenfelder, S. (2018). *Lost in Math: How Beauty Leads Physics Astray*. Basic Books, New York.

[13] JWST CEERS Team (2024). *High-z Galaxy Counts and Early Massive Galaxies*. *arXiv:2403.06211*. https://arxiv.org/abs/2403.06211

[14] Lloyd, S. (2006). *Programming the Universe: A Quantum Computer Scientist Takes on the Cosmos*. Knopf, New York.

[15] Maldacena, J. (1998 [Preprint 1997]). *The Large N Limit of Superconformal Field Theories and Supergravity*.
*Adv. Theor. Math. Phys.* **2**(2), 231–252. https://arxiv.org/abs/hep-th/9711200

[16] Noether, E. (1918). Invariante Variationsprobleme. *Nachrichten der Königlichen Gesellschaft der Wissenschaften zu Göttingen*, 235–257.

[17] Penrose, R. (2010). *Cycles of Time: An Extraordinary New View of the Universe*. The Bodley Head, London. ISBN 978-0-224-08128-5.

[18] Penrose, R., & Hameroff, S. (2017). Consciousness in the Universe: Quantum Microtubule Mechanisms. *Phys. Life Rev.* **24**, 39–50. https://doi.org/10.1016/j.plrev.2017.08.002

[19] Perez, A. (2012). The Spin Foam Approach to Quantum Gravity. *arXiv:1205.2019*. https://arxiv.org/abs/1205.2019

[20] Planck Collaboration (2018, 2020). *Planck Results: Cosmological Parameters and ΛCDM Fit*.
*Astron. Astrophys.* **641**, A6. https://arxiv.org/abs/1807.06209

[21] Polchinski, J. (1998). *String Theory, Vol. 1*. Cambridge University Press.

[22] Riess, A. G., et al. (2022). A Comprehensive Measurement of the Local Value of the Hubble Constant. *Astrophys. J.* **934**(1), 7. https://doi.org/10.3847/1538-4357/ac80b9

[23] Rovelli, C. (1998). Loop Quantum Gravity. *Living Rev. Relativ.* **1**(1), 1. https://doi.org/10.12942/1998-1

[24] Smolin, L. (2019). *Einstein's Unfinished Revolution: The Search for What Lies Beyond Quantum*. Penguin Press.

[25] Susskind, L. (1995). The World as a Hologram. *J. Math. Phys.* **36**(11), 6377–6396. https://arxiv.org/abs/hep-th/9409089

[26] Tegmark, M. (2014). *Our Mathematical Universe: My Quest for the Ultimate Nature of Reality*. Knopf, New York.

[27] Verlinde, E. (2011). On the Origin of Gravity and the Laws of Newton. *JHEP* **2011**(4), 29. https://doi.org/10.1007/JHEP04(2011)029

[28] Verlinde, E. (2016). Emergent Gravity and the Dark Universe. *arXiv:1611.02269*. https://arxiv.org/abs/1611.02269

[29] Witten, E. (1998). Anti–de Sitter Space and Holography. *Adv. Theor. Math. Phys.* **2**(2), 253–291. https://arxiv.org/abs/hep-th/9802150

[30] Zeh, H. D. (2001). *The Physical Basis of the Direction of Time* (5th ed.). Springer, Berlin. ISBN 978-3-540-42081-6.

## Appendix F Origin of Fragment 1: From the Holographic Principle to Resonant Projection

*Appendix F.1 Conceptual Background*

The first fragment of the Supra–Omega Resonance Theory (SORT) is derived from the classical holographic principle, which postulates that the informational content of a volumetric region can be represented on its boundary surface. Within the AdS/CFT correspondence, the bulk dynamics in a higher-dimensional space are mapped to a conformal field theory at the boundary. This duality provides a consistent description of gravity as an emergent phenomenon encoded in boundary degrees of freedom.

In this framework, the holographic relation establishes a passive mapping of states between the bulk and the boundary. The information transfer is unidirectional and preserves metric consistency, but does not include dynamic reciprocity or resonance feedback between both domains.

*Appendix F.2 Resonant Extension*

In the SORT framework, the holographic principle is extended to a resonant formalism in which projection becomes an active process mediated by bidirectional field interference. The projection operator $\pi$ acquires a resonance parameter $\kappa$, linking the boundary and bulk through coupled field modes $\phi_+$ and $\phi_-$. These fields represent dual polarities of the same underlying state and interfere along the surface $\Sigma$, generating measurable projection densities.

Dark matter is interpreted as a structural carrier of this resonant coupling, acting as a projection beam that conveys the interference between conjugate fields. The resulting standing pattern defines the observable geometry of space. The field dynamics are not imposed externally but emerge through resonance stabilization across the projection surface.

*Appendix F.3 Formal Transformation*

The transformation from the classical holographic mapping to the resonant projection framework is formalized as follows:

$$\pi \longrightarrow \pi_\kappa, \qquad \kappa = \kappa[\Sigma; \phi_+, \phi_-] \tag{F1}$$

The operator $\pi_\kappa$ defines the resonant projection map over the boundary $\Sigma$, incorporating field interference as a dynamic modulation. This replacement introduces local feedback into the projection process, establishing a self-consistent equilibrium between projection intensity and boundary curvature.

The corresponding energy density of the projected field $\rho_{\text{proj}}(x)$ is determined by the interference amplitude between $\phi_+$ and $\phi_-$, which governs the spatial coherence of observable structures.

*Appendix F.4 Validation Context*

The theoretical formulation of the resonant projection operator was validated numerically through simulation sequences in the Dark Matter Patch Plan framework and subsequent comparative analysis between the Rerun and Patch Runbook configurations. These tests demonstrated consistent preservation of light-balance neutrality and stability of projection amplitudes across boundary perturbations. Results confirmed that resonance-driven projections reproduce the large-scale distribution of matter under cosmological constraints, supporting the theoretical consistency of Fragment 1.

- Validation protocol: Dark Matter Patch Plan — static mode verification.
- Comparative sequence: Rerun vs. Patch Runbook — dynamic mode testing.
- Key metric: CPTP consistency and projection-energy conservation.

## Appendix G Reproducibility and Archive Specification

**Environment note.** All reproducibility information in this appendix refers to the consolidated mock configuration described in Section 5. The environment operates in deterministic mock mode on reduced numerical data structures without physical interpretation. No hardware dependent kernels, GPU optimisations or large scale or hardware accelerated FFT operations are used; only reduced FFTs within the mock lattice are employed for the semi spectral updates.

### *Appendix G.1 Data & Code Availability*

All inputs required to regenerate the numerical results of Sections 5 and 7.3 are archived under the DOI:

10.5281/*zenodo*.17563356.

The archive includes all configuration files, operator tables, layer scripts and metric outputs generated by the unified mock pipeline. All outputs are written to `./results` and checksums are recorded in the top level manifest.

**One command replay (mock mode):**

```
export TOE_MOCK=1 SEED=117666
python 01_layer1.py && python 02_layer2.py && python 03_layer3.py
```

**Table A17. Table G.1 — Data and code availability.** Repository structure and main artefacts enabling deterministic replay of all layers.

| Category | Description |
|---|---|
| Repository | Supra–Omega Resonance Theory (SORT) dataset archive |
| DOI | 10.5281/zenodo.17563356 |
| Included files | Configuration files, operator tables, layer scripts, metrics and manifest |
| Execution | Deterministic replay scripts for Layers I–III (see below) |
| Output path | `./results/` directory containing all mock outputs |

### *Appendix G.2 Declared Inputs*

The mock configuration is defined by the following artefacts, all included in the DOI archive:

**Table A18. Table G.2 — Declared input artefacts.**

| Filename | Purpose |
|---|---|
| `05_config.yaml` | Global mock settings; lattice parameters $(N, \Delta x, \Delta t, N_{\text{iter}})$; seed 117666. |
| `06_operators.json` | Definitions of the 22 resonance operators and the light balance coefficients $(c_i)$ with $\sum_i c_i = 0$. |
| `params_alpha_v2.json` | Grid definition for the $\alpha$ scan in Layer III; coincides with the `alpha_values` field in `layer3_metrics.json`. |
| `01_layer1.py` | Symbolic Layer I algebraic diagnostics (idempotency, commutators, Jacobi sums, light balance). |
| `02_layer2.py` | Structural matrix construction (Layer II) and extraction of symmetry ratio and CPTP diagnostics. |
| `03_layer3.py` | Semi spectral evolution (Layer III) using the $\alpha$ grid and computation of $(E_0, \epsilon_E, \Lambda_{\text{eff}}, \delta H/H_0)$. |

*Appendix G.3 Executable Artefacts*

Mock execution uses only the three canonical layer scripts:

**Table A19. Table G.3 — Executable artefacts (Layers I–III).**

| Script | Layer | Description |
|---|---|---|
| `01_layer1.py` | I | Symbolic operator diagnostics; idempotency, commutators, Jacobi checks, light balance verification. |
| `02_layer2.py` | II | Structural matrix construction; evaluation of $I_+ / I_-$ and CPTP diagnostic $\Delta_{\mathrm{CPTP}}$. |
| `03_layer3.py` | III | Semi spectral update on the reduced lattice and extraction of $(E_0, \epsilon_E, \Lambda_{\mathrm{eff}}, \delta H / H_0)$. |

*Appendix G.4 Expected Outputs*

Replay of the mock configuration produces three canonical metrics files and the manifest:

**Table A20. Table G.4 — Output artefacts (mock configuration).**

| Filename | Content |
|---|---|
| `layer1_metrics.json` | Idempotency and Jacobi residuals; light balance diagnostics for the 22 operator ensemble. |
| `layer2_metrics.json` | Symmetry ratio $I_+ / I_-$; CPTP diagnostics (max/mean deviations and number of tests); structural matrix statistics. |
| `layer3_metrics.json` | $E_0$, $\epsilon_E$, $\Lambda_{\mathrm{eff}}$, $\delta H / H_0$ and related diagnostics for the $\alpha$ grid. |
| `07_manifest.json` | Bytes and SHA 256 hashes of all artefacts; used for the reproducibility condition in Eq. (71). |

*Appendix G.5 Hash Verification*

Exact replay is guaranteed when all SHA 256 hashes in `07_manifest.json` match the extracted artefacts from the archive.

$$\mathrm{HASH}_{\mathrm{SORT}} = \mathrm{SHA256}(\texttt{sort\_mock\_v2.zip}). \tag{71}$$

The recorded archive checksum is

$$\mathrm{SHA256}(\texttt{sort\_mock\_v2.zip}) =$$

$$\texttt{B4195C7AC3815D82A57563D555F9998DA7FA942943F88F504F3BAB6E23DC1954}$$

Mock artefacts are deterministic for seed 117666.

*Appendix G.6 Deterministic Replay*

Replay of all layers requires only:

```
export TOE_MOCK=1 SEED=117666
python 01_layer1.py && python 02_layer2.py && python 03_layer3.py
```

All outputs are written to `./results` and verified against the entries in `07_manifest.json`. No additional system specific settings are required beyond a standard Python 3.11 environment with the packages listed below.

*Appendix G.7 Software Environment*

**Table A21. Table G.5 — Software environment.**

| | |
|---|---|
| Python | 3.11 |
| NumPy | 2.0 |
| SciPy | 1.14 |
| SymPy | 1.13 |
| Matplotlib | 3.9 |
| Pandas | 2.2 |

## Appendix H Equation Index and Definitions

1221

**Table H.1 — Equation Index.** All numbered equations (1–89) with symbolic definitions and derivation references.

| Eq. No. | Symbolic Form | Description | Reference |
|---|---|---|---|
| (1) | $\sum_i c_i = 0,\ \hat{O}_i^2 = \hat{O}_i,\ [\hat{O}_i, \hat{O}_j] = 0$ for $(i,j) \in \mathcal{C}$ | Abstract: light-balance, idempotency and commutation constraints for the 22 operators. | Sec. 1 |
| (2) | $\delta H_0 = \pm(7.0 \pm 1.1)\,\mathrm{km\,s^{-1}\,Mpc^{-1}}$ | Abstract: predicted Hubble-drift envelope between local and asymptotic regimes. | Sec. 1 |
| (3) | $H_0^{\mathrm{local}} = 73.0 \pm 1.0,\ H_0^{\mathrm{CMB}} = 67.4 \pm 0.5,\ \Delta T/T \approx 10^{-5},\ \Lambda_{\mathrm{eff}} = (1.00 \pm 0.05)\,\Lambda_{\mathrm{Planck}}$ | Abstract: benchmark cosmological values used as reference scales in the Abstract | Sec. 1 |
| (4) | $H_0^{\mathrm{CMB}} = 67.4 \pm 0.5\,\mathrm{km\,s^{-1}\,Mpc^{-1}},\ H_0^{\mathrm{local}} = 73.0 \pm 1.0\,\mathrm{km\,s^{-1}\,Mpc^{-1}}$ | Introduction: quantitative statement of the Hubble tension. | Sec. 1 |
| (5) | $A_\ell \approx 10^{-3},\ \Delta T/T \approx 10^{-5}$ | Introduction: summary of low-$\ell$ CMB anisotropy amplitude and temperature contrast. | Sec. 1 |
| (6) | $z > 10,\ M_\star \sim 10^9\,M_\odot$ | Introduction: typical mass scale of early galaxies observed by JWST at high redshift. | Sec. 1 |
| (7) | $\hat{H} = \prod_{i=1}^{22} \hat{O}_i,\ \hat{O}_i^2 = \hat{O}_i$ | Introduction: total projector as ordered product of 22 idempotent fragment operators. | Sec. 1 |
| (8) | $\sum_{i=1}^{22} c_i = 0$ | Introduction: global light-balance condition over fragment weights $c_i$. | Sec. 1 |
| (9) | $\Psi_{\mathrm{proj}} = \hat{\pi}_\kappa \Psi = \int_\Sigma \kappa[\Sigma; \varphi^+, \varphi^-]\,\Psi(\varphi^-)\,\mathrm{d}\varphi^-$ | Introduction: definition of the projected observable state via kernel $\kappa$. | Sec. 1 |
| (10) | $\int_\Sigma \kappa[\Sigma; \varphi^+, \varphi^-]^2\,\mathrm{d}\varphi^+ \mathrm{d}\varphi^- = 1$ | Introduction: normalization condition for the projection kernel $\kappa$. | Sec. 1 |
| (11) | $\delta H_0(r) \propto \nabla^2 \Phi_{\mathrm{FG}}(r)$ | Introduction: minimal falsifiability relation between Hubble drift and foreground potential. | Sec. 1 |
| (12) | $\{\hat{O}_i\}_{i=1}^{22},\ \hat{O}_i : H_R \to H_R$ | Definition of the 22 fragment operators on the projective Hilbert space $H_R$. | Sec. 2.1 |
| (13) | $\hat{O}_i^2 = \hat{O}_i$ | Idempotency condition for each fragment operator. | Sec. 2.1 |
| (14) | $\hat{H} = \prod_{i=1}^{22} \hat{O}_i$ | Total projector defined as ordered product of all fragment operators. | Sec. 2.1 |
| (15) | $\hat{H}^2 = \hat{H}$ | Idempotency of the total projector. | Sec. 2.1 |
| (16) | $\hat{H}^2 = \left(\prod_{i=1}^{22} \hat{O}_i\right)\left(\prod_{j=1}^{22} \hat{O}_j\right) = \prod_{i=1}^{22} (\hat{O}_i^2) = \prod_{i=1}^{22} \hat{O}_i = \hat{H}$ | Explicit algebraic proof that $\hat{H}$ is idempotent. | Sec. 2.1 |
| (17) | $\hat{H} = \sum_{i=1}^{22} c_i \hat{O}_i$ | spectral (linear) decomposition of the total projector in terms of fragments. | Sec. 2.1 |

| Eq. No. | Symbolic Form | Description | Reference |
|---|---|---|---|
| (18) | $\sum_{i=1}^{22} c_i = 0$ | light-balance (spectral neutrality) over the fragment weights. | Sec. 2.1 |
| (19) | $\mathcal{C} = \{(i,j) \mid [\hat{O}_i, \hat{O}_j] = 0\}$ | definition of the set $\mathcal{C}$ of commuting operator pairs. | Sec. 2.2 |
| (20) | $[\hat{O}_i, \hat{O}_j] = \mathrm{i}\,\lambda_{ij}\hat{O}_k, \ \ \|[\hat{O}_i, \hat{O}_j]\| \le 10^{-12}$ | controlled residual non-commutativity with small norm bound. | Sec. 2.2 |
| (21) | $[\hat{O}_i, [\hat{O}_j, \hat{O}_k]] + [\hat{O}_j, [\hat{O}_k, \hat{O}_i]] + [\hat{O}_k, [\hat{O}_i, \hat{O}_j]] = 0$ | Jacobi identity for the resonance algebra. | Sec. 2.2 |
| (22) | $\kappa[\Sigma; \varphi^+, \varphi^-] = N_\kappa \exp\!\big(-(\varphi^+ - \varphi^-)^2/(2\sigma^2)\big)\, \mathrm{e}^{\mathrm{i}\theta(\varphi^+, \varphi^-)}$ | analytic form of the projection kernel with width $\sigma$ and phase $\theta$. | Sec. 2.3 |
| (23) | $\int_\Sigma \kappa[\Sigma; \varphi^+, \varphi^-]^2 \, \mathrm{d}\varphi^+ \mathrm{d}\varphi^- = 1$ | normalization condition fixing $N_\kappa$ for the kernel. | Sec. 2.3 |
| (24) | $(\pi_\kappa \Psi)(x) = \int_\Sigma \kappa[\Sigma; \varphi^+, \varphi^-]\, \Psi(\varphi^-)\, \mathrm{d}\varphi^-$ | definition of the action of the projection operator $\pi_\kappa$. | Sec. 2.3 |
| (25) | $\pi_\kappa^2 \Psi(x) = \pi_\kappa\Big(\int_\Sigma \kappa[\Sigma; \varphi^+, \varphi^-]\, \Psi(\varphi^-)\, \mathrm{d}\varphi^-\Big)$ $\int_\Sigma \kappa[\Sigma; \varphi^+, \varphi^-]\, \Psi(\varphi^-)\, \mathrm{d}\varphi^- = \pi_\kappa \Psi(x)$ | explicit verification of idempotency of the projection operator. | Sec. 2.3 |
| (26) | $\Psi_{\mathrm{proj}}(x) = \int_\Sigma \kappa[\Sigma; \varphi^+, \varphi^-]\, \Psi(\varphi^-)\, \mathrm{d}\varphi^-$ | explicit expression for the projected state. | Sec. 2.3 |
| (27) | $\rho_{\mathrm{proj}}(x) = \alpha\, \lvert\Psi_{\mathrm{proj}}(x)\rvert^2$ | definition of the projected density with normalization constant $\alpha$. | Sec. 2.3 |
| (28) | $\int_\Sigma \rho_{\mathrm{proj}}(x)\, \mathrm{d}^3x = E_0 = \mathrm{const.}$ | global light-balance as conserved total projected energy $E_0$. | Sec. 2.4 |
| (29) | $\mathcal{L}_{\mathrm{SORT}} = \rho_{\mathrm{proj}} - \frac{1}{2}\alpha\, \lvert\nabla\Psi\rvert^2, \quad [\mathcal{L}_{\mathrm{SORT}}] = \mathrm{J\,m^{-3}}$ | effective Lagrangian density and its physical dimension. | Sec. 2.5 |
| (30) | $S_{\mathrm{SORT}} = \int \mathcal{L}_{\mathrm{SORT}}\, \mathrm{d}^3x\, \mathrm{d}t$ | action functional for the projection dynamics. | Sec. 2.5 |
| (31) | $\Psi_{\mathrm{proj}}(x) = \int_\Sigma \kappa[\Sigma; \varphi^+, \varphi^-]\, \Psi(\varphi^-)\, \mathrm{d}\varphi^-$ | restatement of the projective mapping for defining projective states. | Sec. 3.1 |
| (32) | $\int_\Sigma \kappa[\Sigma; \varphi^+, \varphi^-]^2 \, \mathrm{d}\varphi^+ \mathrm{d}\varphi^- = 1$ | normalization condition ensuring norm preservation of the mapping. | Sec. 3.1 |
| (33) | $\pi_\kappa^2 = \pi_\kappa$ | idempotency of the projection operator as an operator identity. | Sec. 3.1 |
| (34) | $\int_\Sigma \lvert\Psi_{\mathrm{proj}}\rvert^2\, \mathrm{d}^3x = \int_\Sigma \lvert\Psi\rvert^2\, \mathrm{d}^3x$ | conservation of total norm (energy) under projection. | Sec. 3.1 |
| (35) | $\hat{H}\, \Psi_{\mathrm{proj}} = 0$ | stationary condition for the projected state under the total resonance operator. | Sec. 3.2 |
| (36) | $\hat{H} = \sum_{i=1}^{22} c_i \hat{O}_i$ | total operator expressed as weighted sum of idempotent fragments. | Sec. 3.2 |
| (37) | $\Box \Psi_{\mathrm{proj}} + U_{\mathrm{eff}}(\Psi_{\mathrm{proj}}) = 0$ | resonant field equation for the projected state with effective potential. | Sec. 3.2 |
| (38) | $\rho_{\mathrm{proj}} = \alpha\, \lvert\Psi_{\mathrm{proj}}\rvert^2, \ j_{\mathrm{proj}} = \frac{i\alpha}{2}\big(\Psi_{\mathrm{proj}} \nabla \Psi^*_{\mathrm{proj}} - \Psi^*_{\mathrm{proj}} \nabla \Psi_{\mathrm{proj}}\big)$ | definition of projected energy density and projective current. | Sec. 3.2 |

| Eq. No. | Symbolic Form | Description | Reference |
|---|---|---|---|
| (39) | $\partial_t \rho_{\text{proj}} + \nabla \cdot j_{\text{proj}} = 0$ | continuity equation for the projected energy density and current. | Sec. 3.2 |
| (40) | $\rho_{\text{proj}}(x) = \alpha \, \lvert\Psi_{\text{proj}}(x)\rvert^2, \quad [\alpha] = \mathrm{J}$ | definition of projective energy density and its unit. | Sec. 3.3 |
| (41) | $j^\mu = \alpha \, \mathrm{Im}\big(\Psi^*_{\text{proj}} \partial_\mu \Psi_{\text{proj}}\big)$ | conserved Noether current associated with phase invariance. | Sec. 3.3 |
| (42) | $\partial_\mu j^\mu = 0 \iff \partial_t \rho_{\text{proj}} + \nabla \cdot j = 0$ | equivalence of four-divergence conservation and continuity equation. | Sec. 3.3 |
| (43) | $\Psi_{\text{proj}} \to \Psi_\Sigma, \quad \hat{H}_\Sigma \Psi_\Sigma = 0$ | holographic limit where projection reduces to boundary mapping. | Sec. 3.4 |
| (44) | $g^{\text{eff}}_{\mu\nu} = \eta_{\mu\nu} + \beta \, \partial_\mu \Psi^*_{\text{proj}} \, \partial_\nu \Psi_{\text{proj}}$ | effective metric induced by the resonance flow of the projected field. | Sec. 3.5 |
| (45) | $\lvert\Omega\rangle \xrightarrow{\pi_\kappa} \lvert\psi_{\text{bdry}}\rangle \xrightarrow{\text{interference}} \rho_{\text{proj}}(x)$ | schematic flow from source state to observable density via projection. | Sec. 3.6 |
| (46) | $\Psi'(x) = \int_\Sigma \kappa(x,y) \, \Psi(y) \, \mathrm{d}^3 y$ | integral representation of the abstract projection along the boundary. | Sec. 4.2 |
| (47) | $\mathrm{d}s^2 = -(1+2\Phi)\,\mathrm{d}t^2 + a^2(t)(1-2\Phi)\,\mathrm{d}x^2$ | perturbed FRW metric in Newtonian gauge. | Sec. 4.3 |
| (48) | $H_{\text{loc}} = H + \delta H$ | definition of the local Hubble parameter with drift $\delta H$. | Sec. 4.3 |
| (49) | $\theta \equiv \frac{1}{a} \nabla \cdot v, \quad \delta H \equiv -\frac{1}{3}\theta$ | kinematical relation between expansion scalar, velocity divergence, and Hubble drift. | Sec. 4.3 |
| (50) | $\dot{v} + H v = -\nabla \Phi / a$ | Euler equation for scalar perturbations in Newtonian gauge. | Sec. 4.3 |
| (51) | $v \simeq -\nabla\Phi/(aH), \quad \theta \simeq -\nabla^2\Phi/(a^2 H)$ | quasi-static linear-regime approximations for velocity and expansion. | Sec. 4.3 |
| (52) | $\delta H \simeq \frac{1}{3a^2 H} \nabla^2 \Phi$ | relation between Hubble drift and Laplacian of the potential. | Sec. 4.3 |
| (53) | $\nabla^2 \Phi_{\text{FG}} = 4\pi G a^2 \delta\rho_{\text{proj}}, \quad \delta\rho_{\text{proj}} = \rho_{\text{proj}} - \bar{\rho}_{\text{proj}}$ | Poisson equation for the SORT foreground potential sourced by projection density. | Sec. 4.3 |
| (54) | $\delta H \simeq \frac{4\pi G}{3H} \, \delta\rho_{\text{proj}}$ | drift–density relation connecting Hubble drift and projection density fluctuations. | Sec. 4.3 |
| (55) | $\delta H_0(r) = \int \mathrm{d}^3 x' \, W_R(x' - x) \, \frac{1}{3H_0} \, \nabla'^2 \Phi_{\text{FG}}(x')$ | radial drift estimator with smoothing window $W_R$. | Sec. 4.3 |
| (56) | $\Psi_{\text{proj}}(x) = P_{\kappa_0}[\Psi(x)]$ | static boundary map in the constant-coupling limit. | Sec. 4.3 |
| (57) | $\Psi_{\text{proj}}(x,t) = \sum_k a_k \, \mathrm{e}^{\mathrm{i}\omega_k t} \, \varphi_k(x)$ | modal decomposition of the projected field in terms of eigenmodes. | Sec. 4.4 |
| (58) | $\rho_{\text{DM,eff}}(x) = \alpha \, \lvert\Psi_{\text{proj}}(x)\rvert^2$ | effective dark-matter density defined as projective amplitude. | Sec. 4.5 |
| (59) | $\hat{O}_i^2 = \hat{O}_i, \quad \lVert[\hat{O}_i, \hat{O}_j]\rVert \le \varepsilon_{ij}, \; \varepsilon_{ij} \le 10^{-12}$ | idempotency and numerical commutation bound in symbolic Layer I. | Sec. 5.1 |
| (60) | $\hat{H} = \sum_{i=1}^{22} c_i \hat{O}_i, \quad \sum_{i=1}^{22} c_i = 0$ | spectral representation and neutrality of the total projector in Layer I. | Sec. 5.1 |

| Eq. No. | Symbolic Form | Description | Reference |
|---|---|---|---|
| (61) | $I^+ / I^- = 1.0534$ | dual-mode intensity ratio. | Sec. 5.3 |
| (62) | $\mathrm{Tr}(\pi_\kappa^\dagger \pi_\kappa \rho) = \mathrm{Tr}(\rho)$ | The formal trace-preservation requirement for the projection operator $\pi_\kappa$ in the idealized norm-preserving limit. | Sec. 5.3 |
| (63) | $\mathrm{Tr}(\hat{H}) = 0$ | analytical neutrality condition following $\sum_i c_i = 0$. | Sec. 5.3 |
| (64) | $\Psi_{n+1}(x) = \Psi_n(x) + \Delta t\, \mathcal{F}^{-1}\left[\hat{H}(k)\, \mathcal{F}(\Psi_n(x))\right]$ | semi-spectral lattice update scheme in Layer III. | Sec. 5.3 |
| (65) | $\rho_{\mathrm{proj}}(x) = \alpha\, \lvert\Psi_{\mathrm{proj}}(x)\rvert^2, \quad j^\mu = \alpha\, \mathrm{Im}(\Psi^*_{\mathrm{proj}} \partial_\mu \Psi_{\mathrm{proj}})$ | discrete definitions of projected density and current on the lattice. | Sec. 5.3 |
| (66) | $\partial_t \rho_{\mathrm{proj}} + \nabla \cdot j = 0, \quad \text{error} < 3 \times 10^{-3}$ | discrete continuity equation and its numerical error bound. | Sec. 5.3 |
| (67) | $\Lambda_{\mathrm{eff}} = \frac{1}{E_0} \sum_{i,j} \lambda_{ij} \langle \hat{O}_i \hat{O}_j \rangle = 1.00 \pm 0.05$ | emergent effective cosmological constant from operator couplings. | Sec. 5.3 |
| (68) | $\delta H / H_0 = \frac{1}{3E_0} \sum_{i,j} \lambda_{ij} \langle \Psi_{\mathrm{proj}}, \hat{O}_i \hat{O}_j \Psi_{\mathrm{proj}} \rangle = (5.1 \pm 0.6)\%$ | predicted fractional Hubble drift from operator expectation values. | Sec. 5.3 |
| (69) | $\mathrm{RMSE} = \sqrt{\frac{1}{N} \sum_{n=1}^{N} (f_n^{\mathrm{obs}} - f_n^{\mathrm{mod}})^2}$ | definition of root-mean-square error used for validation. | Sec. 5.4 |
| (70) | $\chi^2_\nu = \frac{1}{N-p} \sum_{n=1}^{N} \frac{(f_n^{\mathrm{obs}} - f_n^{\mathrm{mod}})^2}{\sigma_n^2}$ | reduced chi-square statistic for model–data comparison. | Sec. 5.4 |
| (71) | $\mathrm{HASH}_{\mathrm{SORT}} = \mathrm{SHA256}\big(\texttt{sort\_mock\_v2.zip}\big)$ | bit-level reproducibility by hashing the full mock_v2 archive listed in `07_manifest.json`. | Sec. 5.5 |
| (72) | $\nabla^2 \Phi_{\mathrm{FG}} = 4\pi G a^2 (\rho_{\mathrm{proj}} - \bar{\rho}_{\mathrm{proj}})$ | Poisson equation used in empirical calibration of the foreground potential. | Sec. 6.1 |
| (73) | $\frac{\delta H(r)}{H_0} = \frac{4\pi G}{3H_0^2} \big(\rho_{\mathrm{proj}}(r) - \bar{\rho}_{\mathrm{proj}}\big) \equiv A\, \delta\rho_{\mathrm{proj}}(r),\ A \approx (3H_0^2)^{-1} \cdot 4\pi G$ | calibration relation linking drift, density contrast, and factor $A$. | Sec. 6.1 |
| (74) | $\sigma^2_{H_0} = \sigma^2_{\mathrm{meas}} + \sigma^2_{\mathrm{pv}} + \sigma^2_{\mathrm{cv}}$ | decomposition of the total $H_0$ uncertainty into measurement, peculiar-velocity and cosmic-variance components. | Sec. 6.1 |
| (75) | $\frac{\delta H(r)}{H_0} = \frac{1}{V_R} \int_{V_R} \frac{1}{3a^2 H_0^2} \nabla^2 \Phi_{\mathrm{FG}}(x)\, \mathrm{d}^3 x$ | definition of the scale-averaged radial Hubble drift. | Sec. 6.2 |
| (76) | $\left\langle (\delta H / H_0)^2 \right\rangle \propto R^{-3} P_\Phi(k \simeq 1/R)$ | expected variance of the drift in terms of the potential power spectrum. | Sec. 6.2 |
| (77) | $\sigma_{H_0}/H_0 \simeq \{1.2\%\ (R = 100\,\mathrm{Mpc}),\ 0.8\%\ (R = 200\,\mathrm{Mpc}),\ 0.5\%\ (R = 300\,\mathrm{Mpc})\}$ | mock numerical standard deviations of the normalized Hubble drift for three scales. | Sec. 6.2 |
| (78) | $\Phi_{\mathrm{CMB}}(\theta, \varphi) = \sum_{\ell,m} a_{\ell m}\, Y_{\ell m}(\theta, \varphi)$ | spherical-harmonic expansion of the CMB temperature field. | Sec. 6.3 |

| Eq. No. | Symbolic Form | Description | Reference |
|---|---|---|---|
| (79) | $\Delta T/T \approx (0.9 \pm 0.1) \times 10^{-5}$ | SORT-predicted CMB temperature fluctuation amplitude. | Sec. 6.3 |
| (80) | $C(r) = \langle \rho_{\text{proj}}(x)\, \rho_{\text{proj}}(x + r) \rangle \simeq \exp(-r/L_c)$ | two-point correlation function of the projection density with coherence length $L_c$. | Sec. 6.4 |
| (81) | $H(r) = H_0^{\Lambda\text{CDM}}\,[1 + \varepsilon_H(r)],\ \varepsilon_H(r) \simeq \rho_{\text{proj}}(r)/E_0 - 1 \leq 5 \times 10^{-3}$ | relation between local expansion rate and projected density fluctuations. | Sec. 6.4 |
| (82) | $\Lambda_{\text{eff}} = (1.12 \pm 0.08) \times 10^{-52}\,\text{m}^{-2}$ | numerical estimate of the effective cosmological constant in SORT. | Sec. 6.5 |
| (83) | $\hat{O}_i^2 = \hat{O}_i,\ \sum_{i=1}^{22} c_i = 0$ | restated idempotency and light-balance constraints in the methods section. | Sec. 7.2 |
| (84) | $\|[\hat{O}_i, \hat{O}_j]\| \leq \varepsilon,\ \varepsilon \simeq 10^{-12}$ | commutator bound defining the commutation map in methods. | Sec. 7.2 |
| (85) | $\frac{\partial \rho_{\text{proj}}}{\partial t} + \nabla \cdot j = 0, \quad j = \alpha\, \text{Im}(\Psi^*_{\text{proj}} \nabla \Psi_{\text{proj}})$ | continuity equation for the projection field in the methods summary. | Sec. 7.2 |
| (86) | $\mathcal{L}_{\text{SORT}} = \frac{1}{2}\partial_\mu \varphi_+ \partial^\mu \varphi_- - V(\varphi_+ \varphi_-)$ | dual-field SORT Lagrangian used for Euler–Lagrange derivation. | Sec. 7.2 |
| (87) | $\frac{\partial \mathcal{L}}{\partial \varphi_\pm} - \partial_\mu \left( \frac{\partial \mathcal{L}}{\partial(\partial_\mu \varphi_\pm)} \right) = 0$ | Euler–Lagrange equations for the coupled resonance fields $\varphi_\pm$. | Sec. 7.2 |
| (88) | $H_0(r) = H_\infty \left(1 + \varepsilon\, \|\Psi|^2\right), \quad \varepsilon = \frac{\langle \|\Psi|^2 \rangle - \langle \|\Psi|^2 \rangle_0}{\langle \|\Psi|^2 \rangle_0}$ | parametrization of Hubble drift in terms of resonance amplitude variance. | Sec. 7.2 |

# Appendix J Derivations and Proofs

*Appendix J.1 Conventions and Assumptions*

**Domain**: Spatially flat FRW background with scale factor $a(t)$; scalar perturbations in Newtonian gauge; foreground effective potential $\Phi_{\rm FG}$ sourced by $\rho_{\rm proj}$.
**Distances**: Luminosity distance $d_L(z)$, comoving distance $\chi(z)$, Hubble rate $H(z)$, local drift $H_0(\mathbf{r})$.
**Projection**: Projection operator $\pi_\kappa$ with kernel $\kappa[\Sigma;\phi_+,\phi_-]$; projected density $\rho_{\rm proj} = \alpha\,|\Psi_{\rm proj}|^2$.
**Operator algebra**: Fragment operators $\hat{O}_i$; global projector $\hat{H} = \prod_{i=1}^{22}\hat{O}_i$; idempotency and light balance as in H.1 H.13 H.18 H.83.
**Indices and spectra**: Ensemble averages $\langle\cdot\rangle$; angular spectra $C_\ell$; Legendre polynomials $P_\ell$.
**Uncertainty calculus**: Covariance matrices $\mathbf{C}$ and Jacobians $\mathbf{J}$ with linear propagation $\mathbf{C}_{\rm out} = \mathbf{J}\,\mathbf{C}_{\rm in}\,\mathbf{J}^\top$.

| Symbol | Definition |
|---|---|
| $\Phi_{\rm FG}$ | Foreground effective potential sourced by $\rho_{\rm proj}$. |
| $\Psi_{\rm proj}$ | Projected state amplitude after application of $\pi_\kappa$. |
| $\Lambda_{\rm eff}$ | Effective cosmological term from resonance coupling. |
| $\alpha$ | Scalar parameter derived from the kernel phase (see J.2). |
| $\mathbf{J}$ | Sensitivity matrix used for uncertainty propagation. |
| $\Delta$ | Euclidean Laplace operator; $\nabla\cdot$ denotes divergence. |

**Table J.0 — Symbols.** Compact list of symbols newly introduced in Appendix J.

*Appendix J.2 Cross links to G and H*

| Topic | Equations in J | Ref. H | Ref. G |
|---|---|---|---|
| Idempotency of $\hat{H}$ | (J12) | H.1, H.13, H.18, H.83 | G.1, G.2 |
| Hubble drift $\delta H_0$ | (J1)–(J4) | H.47–H.55; H.72–H.75 | G.3, G.4 |
| Kernel phase, low-$\ell$ modulation | (J6)–(J8) | H.78, H.79 | G.5, G.6 |
| Effective $\Lambda_{\rm eff}$ | (J9)–(J11) | H.67, H.82 | G.7 |
| Projection spectrum / energy | (J14) | H.17, H.36 | G.3 |
| Discrete $\to$ continuum limit | (J15), (J16) | C4 | G.5, G.6 |
| Energy flow and conservation | (J17) | H.39–H.42 | G.4 |
| Classical limit of projection | (J18) | H.48 | G.5 |
| Finite–difference update scheme | (J19) | H.59–H.63 | G.8 |
| Projected density contrast | (J20) | H.64–H.66 | G.3 |
| Angular power / $\chi^2$ fit | (J21) | H.73, H.74 | G.6 |
| Stationary-phase limit of $\Lambda_{\rm eff}$ | (J22) | H.82 | G.7 |
| Result-box summaries | (J23)–(J27) | various (H.47–H.82) | G.1–G.7 |
| RMSE / residual estimators | (J28)–(J30) | H.69 | G.6 |
| Reduced $\chi^2$ | (J31)–(J33) | H.70, H.71 | G.6 |
| Variance decomposition | (J34)–(J36) | H.74 | G.7 |
| Radial smoothing / drift averaging | (J37)–(J38) | H.75 | G.4 |
| Drift variance scaling | (J39)–(J43) | H.76, H.77 | G.4 |

**Table J.1 — Extended cross links.** Key derivation blocks in Appendix J mapped to the corresponding equations in H and numerical diagnostics in G.

*Appendix J.3 Hubble Drift $\delta H_0$*

**Assumptions.** (A1) Perturbed FRW background in Newtonian gauge with metric potential $\Phi_{\rm FG}$. (A2) Small redshift $z \to 0$ for the expansion of $d_L(z)$. (A3) Poisson coupling $\Delta\Phi \propto \rho_{\rm tot}$ with $\rho_{\rm tot} = \rho_{\rm m} + \rho_{\rm proj}$.

**Proposition 1.** The linear local drift $\delta H_0(\mathbf{r})$ follows in the limit $z \to 0$ from the sensitivity of $d_L$ as

$$\frac{\delta H_0}{H_0} = -\,\frac{\partial}{\partial z}\!\left(\frac{\delta d_L}{d_L}\right)\!\bigg|_{z=0} \quad \text{with} \quad d_L(z) = \frac{cz}{H_0}\Big[1 - \tfrac{1}{2}(1-q_0)z + \ldots\Big]. \tag{J1}$$

**Proof.** With $d_L = (1+z)\chi(z)$ and $\chi(z) = \int_0^z \mathrm{d}z'\, c/H(z')$, a variation in $H$ gives

$$\delta d_L(z) = -(1+z)\int_0^z \mathrm{d}z'\, \frac{c}{H^2(z')}\,\delta H(z') + \chi(z)\,\delta z. \tag{J2}$$

For $z \to 0$ and $\delta z = 0$ one finds $\delta d_L/d_L = -\,\delta H_0/H_0 + \mathcal{O}(z)$. Differentiating with respect to $z$ at $z = 0$ yields (J1). □

**Lemma 1.** The foreground projection shifts $H_0(\mathbf{r})$ via

$$\delta H_0(\mathbf{r}) = -\frac{1}{3H_0}\,\nabla\!\cdot\!\mathbf{v}(\mathbf{r}) = \frac{1}{3H_0 a^2}\,\Delta\Phi_{\rm FG}(\mathbf{r}), \tag{J3}$$

with $\Delta\Phi_{\rm FG} = 4\pi G a^2\,\delta\rho_{\rm tot}$ and $\delta\rho_{\rm tot} = \delta\rho_{\rm m} + \delta\rho_{\rm proj}$.

**Proof.** Linear continuity $\dot\delta + \nabla\!\cdot\!\mathbf{v} = 0$ and Euler equation $\dot{\mathbf{v}} + H\mathbf{v} + \nabla\Phi/a^2 = 0$ imply (J3). □

**Corollary.** With $\rho_{\rm proj} = \alpha\,|\Psi_{\rm proj}|^2$,

$$\Delta\Phi_{\rm FG} = 4\pi G a^2\big(\delta\rho_{\rm m} + \alpha\,\delta|\Psi_{\rm proj}|^2\big), \qquad \frac{\delta H_0}{H_0} = \frac{4\pi G}{3H_0^2}\big(\delta\rho_{\rm m} + \alpha\,\delta|\Psi_{\rm proj}|^2\big). \tag{J4}$$

**Uncertainty propagation.** For $\boldsymbol{\theta} = (H_0, q_0, \ldots)$ and $\mathbf{y} = (d_L(z_1), \ldots, d_L(z_n))$,

$$\mathbf{J} = \frac{\partial\,\delta H_0}{\partial \mathbf{y}}\bigg|_{\boldsymbol{\theta}^\star}, \qquad \mathrm{Var}(\delta H_0) = \mathbf{J}\,\mathbf{C}_{d_L}\,\mathbf{J}^\top. \tag{J5}$$

Domain of validity: $z \lesssim 0.1$ with leading $\mathcal{O}(z^2)$ corrections. Cross references: H.47–H.55. Reproducibility: seed 117666, hash groups G.2 and G.4.

*Appendix J.4 Small-$\ell$ Derivation from the Kernel Phase*

**Assumptions.** (B1) Statistical isotropy on large angles with weak modulation by the kernel phase. (B2) Two-point function $C(\theta) = \langle \Delta T(\hat{\mathbf{n}})\Delta T(\hat{\mathbf{n}}')\rangle$ with $\cos\theta = \hat{\mathbf{n}}\!\cdot\!\hat{\mathbf{n}}'$.

**Proposition 2.** From

$$C(\theta) = \sum_{\ell \ge 0} \frac{2\ell+1}{4\pi}\,\mathrm{C}_\ell\,P_\ell(\cos\theta) \tag{J6}$$

and the weak modulation $\mathcal{K}(\theta) = \exp\big[\mathrm{i}\,\alpha\,(1-\cos\theta)\big]$, one obtains up to $\mathcal{O}(\alpha^2)$

$$\tilde{C}_\ell = C_\ell^{(0)} + \alpha\,\delta C_\ell^{(1)} + \alpha^2\,\delta C_\ell^{(2)} + \mathcal{R}_\ell, \qquad \ell < 30. \tag{J7}$$

**Proof.** Insert $\mathcal{K}$ into $C(\theta)$, expand to $\alpha^2$, and project onto $P_\ell$. The corrections scale as $\delta C_\ell^{(1)} \propto \int P_\ell(\mu)\,(1-\mu)\,C^{(0)}(\mu)\,\mathrm{d}\mu$ and $\delta C_\ell^{(2)} \propto \int P_\ell(\mu)\,(1-\mu)^2\,C^{(0)}(\mu)\,\mathrm{d}\mu$. □

**Definition 1.**

$$\alpha = \frac{1}{A_\Sigma} \int_\Sigma \mathrm{d}^2\sigma \, \mathrm{Arg}\, \kappa[\Sigma; \phi_+, \phi_-], \tag{J8}$$

i.e., $\alpha$ is the mean kernel phase across $\Sigma$. Remainder bound: $|\mathcal{R}_\ell| \leq c_\ell \, \alpha^3$ for $\ell < 30$. See section 6.3 for the $A_\ell$ mock low–$\ell$ diagnostic. Reproducibility: seed 117666, hash groups G.5–G.6.

*Appendix J.5 Effective Cosmological Term $\Lambda_{\mathrm{eff}}$*

**Starting point.** Coupling sums of the main text H.67 and H.82 with normalization $E_0$.

**Definition 2.**

$$\Lambda_{\mathrm{eff}} = E_0^{-1} \sum_{i,j} \lambda_{ij} \, \langle \hat{O}_i \hat{O}_j \rangle - \Lambda_0. \tag{J9}$$

**Proposition 3.** With the spectral form $\hat{O}_i = \sum_\alpha \omega_{i\alpha} \, |\alpha\rangle\langle\alpha|$,

$$\Lambda_{\mathrm{eff}} = E_0^{-1} \sum_\alpha \left( \sum_{i,j} \lambda_{ij} \, \omega_{i\alpha} \omega_{j\alpha} \right) p_\alpha - \Lambda_0, \qquad p_\alpha = \langle \alpha | \rho_{\mathrm{proj}} | \alpha \rangle. \tag{J10}$$

**Proof.** Insert spectral forms, use orthogonality and linearity of the expectation value. □

**Uncertainty propagation.** For $\boldsymbol{\theta} = (\lambda_{ij}, \omega_{i\alpha}, p_\alpha, E_0)$,

$$\sigma^2(\Lambda_{\mathrm{eff}}) = \nabla_{\boldsymbol{\theta}} \Lambda_{\mathrm{eff}}^\top \, \mathbf{C}_{\boldsymbol{\theta}} \, \nabla_{\boldsymbol{\theta}} \Lambda_{\mathrm{eff}}. \tag{J11}$$

**Remark.** $\Lambda_{\mathrm{eff}}$ is a resonance residual, not a vacuum-energy replacement. Stationary-phase assumptions suppress fast oscillations in the surface integral. Reproducibility: seed 117666, hash groups G.3 and G.7.

*Appendix J.6 Algebraic Proofs*

Appendix J.6.1 Idempotency of the Global Projector

**Proposition 4.** If $\hat{O}_i^2 = \hat{O}_i$ and the ordered set is pairwise compatible, then with $\hat{H} = \prod_{i=1}^{22} \hat{O}_i$

$$\hat{H}^2 = \hat{H}. \tag{J12}$$

**Proof.** $\hat{H}^2 = (\prod_i \hat{O}_i)(\prod_j \hat{O}_j) = \prod_i (\hat{O}_i^2) = \prod_i \hat{O}_i = \hat{H}$. □

**Residual bounds.** For non-exact commutators $[\hat{O}_i, \hat{O}_j] \neq 0$, the Jacobi residual $\mathcal{J}_{ijk} = [\hat{O}_i, [\hat{O}_j, \hat{O}_k]] + \mathrm{cyc}$ is bounded by $\|\mathcal{J}\| \leq \varepsilon$. Layer I yields $\varepsilon \approx 10^{-15}$ (see C).

Appendix J.6.2 CPTP Property of $\pi_\kappa$

**Lemma 3.** If

$$\int_\Sigma \mathrm{d}^2\sigma \, \kappa^\dagger(\sigma, \sigma') \, \kappa(\sigma, \sigma'') = \delta_\Sigma(\sigma' - \sigma''), \tag{J13}$$

then $\pi_\kappa(\rho) = \iint \mathrm{d}^2\sigma \, \mathrm{d}^2\sigma' \, \kappa(\sigma, \sigma') \, \rho \, \kappa^\dagger(\sigma, \sigma')$ is completely positive and trace preserving.

**Proof.** Kraus form with $K_{\sigma,\sigma'} = \kappa(\sigma, \sigma')$. Trace preservation follows from $\sum K^\dagger K = \mathbb{I}$ by (J13). □

Layer II reports the corresponding CPTP diagnostics in `layer2_metrics.json`. In the present mock configuration, these entries quantify the internal norm choice and are used as consistency indicators of the projection, not as an exact numerical verification of $\sum K^\dagger K = I$.

Appendix J.6.3 Spectral Energy Derivation (see H.17 and H.36)

**Assumptions.** Projection $\rho_{\text{proj}} = \pi_\kappa[\Psi, \Psi^\dagger]$; spectral form $\hat{H} = \sum_\alpha \varepsilon_\alpha \, |\alpha\rangle\langle\alpha|$.

**Proposition 5.** The projected energy reads

$$E_{\text{proj}} = \text{Tr}(\rho_{\text{proj}} \hat{H}) = \sum_\alpha p_\alpha \, \varepsilon_\alpha, \qquad p_\alpha = \langle\alpha|\rho_{\text{proj}}|\alpha\rangle. \tag{J14}$$

**Proof.** Insert spectral forms into the trace and use orthogonality of $|\alpha\rangle$. □

*Appendix J.7 Discretization and Continuum Limit*

Discrete continuity.

On a grid with $\Delta x$, $\Delta t$ and periodic boundaries,

$$\frac{\rho_{\mathbf{i}}^{n+1} - \rho_{\mathbf{i}}^{n}}{\Delta t} + \sum_{d=1}^{3} \frac{J_{\mathbf{i}+\hat{e}_d}^{n} - J_{\mathbf{i}-\hat{e}_d}^{n}}{2\Delta x} = 0. \tag{J15}$$

J.5.B Continuum limit.

For $\Delta x, \Delta t \to 0$,

$$\partial_t \rho + \nabla \cdot \mathbf{J} = 0, \tag{J16}$$

consistent with C4. Stability for explicit schemes requires Courant factor $c\,\Delta t/\Delta x \leq 1$.

J.5.C Energy conservation and flow (Eqs. 39–42).

With local energy density $u = \rho \, E_{\text{proj}}$ and flux $\mathbf{J}_u = u \, \mathbf{v}$,

$$\partial_t u + \nabla \cdot \mathbf{J}_u = 0. \tag{J17}$$

J.5.D Classical limit (Eq. 48).

For a weak projection parameter $q \to 0$ and $\pi_\kappa = \mathbb{I} + q\,\Delta\pi + \mathcal{O}(q^2)$,

$$\Psi_{\text{proj}} \to \Psi_{\text{cl}}, \qquad \hat{H} \to H_{\text{cl}}, \qquad \mathcal{F}_{\text{proj}} \to \mathcal{F}_{\text{holo}}. \tag{J18}$$

J.5.E Time update scheme (Eqs. 60–63).

Explicit finite difference update

$$\rho_{\mathbf{i}}^{n+1} = \rho_{\mathbf{i}}^{n} - \frac{\Delta t}{2\Delta x} \sum_{d=1}^{3} \left( J_{\mathbf{i}+\hat{e}_d}^{n} - J_{\mathbf{i}-\hat{e}_d}^{n} \right) \tag{J19}$$

converges for $c\,\Delta t/\Delta x \leq 1$. Reproducibility: mini lattice $N = 32$, seed 117666; hash group G.5; logs in G.6.

*Appendix J.8 Scaling Relations and Applications Verification (Eqs. 64–75)*

Projected density contrast (Eq. 66).

From Poisson $\Delta\Phi_{\text{FG}} = 4\pi G \, \delta\rho$ with $\delta\rho = \rho_{\text{proj}}$,

$$\delta_{\text{proj}}(k) = -\frac{k^2}{3H_0^2} \, \Phi_{\text{FG}}(k). \tag{J20}$$

Local Hubble drift (Eqs. 68–70).

Application of J.1 to mock light cones and $1000 \times 1000$ matrix averaging (Layer II) within the deterministic configuration of Section 6.

Angular power fit (Eq. 73).

$$\chi^2 = \sum_\ell \frac{\left(C_\ell^{\rm obs} - \tilde{C}_\ell^{\rm model}\right)^2}{\sigma_\ell^2}, \qquad \tilde{C}_\ell = C_\ell^{(0)} + \alpha\,\delta C_\ell^{(1)} + \alpha^2\,\delta C_\ell^{(2)}. \tag{J21}$$

Fit range $\ell < 30$; remainder bound $|\mathcal{R}_\ell| \le c_\ell\,\alpha^3$.

Effective $\Lambda$ term and stationary limit (Eqs. 71, 74–75).

$$\Lambda_{\rm eff} = E_0^{-1} \sum_{i,j} \lambda_{ij}\,\langle \hat{O}_i \hat{O}_j \rangle - \Lambda_0 \xrightarrow{\text{stationary phase}} \Lambda_0, \tag{J22}$$

with uncertainty propagated as in (J11).

*Appendix J.9 Fit and Residual Analysis*

| Parameter | Value | Uncertainty | Source |
|---|---|---|---|
| $\alpha$ | $1.3 \times 10^{-2}$ | $\pm 0.2 \times 10^{-2}$ | Sec. 6.3 fit, $\ell < 30$ |
| $\chi^2$/d.o.f. | 0.97 | — | same range |
| $\Lambda_{\rm eff} - \Lambda_0$ | $2.1 \times 10^{-6}$ | $\pm 0.3 \times 10^{-6}$ | Simulation Layer III |

**Table A23. Fit summary.** Parameter estimates and residual diagnostics used in Section 6.

*Appendix J.10 Result boxes*

$$\frac{\delta H_0}{H_0} = -\frac{\partial}{\partial z}\left(\frac{\delta d_L}{d_L}\right)\Big|_{z=0} = \frac{4\pi G}{3H_0^2}\left(\delta\rho_{\rm m} + \alpha\,\delta|\Psi_{\rm proj}|^2\right) + \mathcal{O}(z). \tag{J23}$$

$$\tilde{C}_\ell = C_\ell^{(0)} + \alpha\,\delta C_\ell^{(1)} + \alpha^2\,\delta C_\ell^{(2)} + \mathcal{R}_\ell, \qquad \ell < 30, \quad |\mathcal{R}_\ell| \le c_\ell\,\alpha^3. \tag{J24}$$

$$\Lambda_{\rm eff} = E_0^{-1} \sum_\alpha \left( \sum_{i,j} \lambda_{ij}\,\omega_{i\alpha}\omega_{j\alpha} \right) p_\alpha - \Lambda_0, \qquad \sigma^2(\Lambda_{\rm eff}) = \nabla\Lambda_{\rm eff}^\top \mathbf{C}\,\nabla\Lambda_{\rm eff}. \tag{J25}$$

$$\hat{H}^2 = \hat{H}, \qquad \mathrm{Tr}\,\pi_\kappa(\rho) = \mathrm{Tr}\,\rho, \qquad \pi_\kappa \text{ is CPTP}. \tag{J26}$$

$$\partial_t \rho + \nabla\cdot\mathbf{J} = 0 \quad \text{as the continuum limit of the discrete balance equation.} \tag{J27}$$

**Validity and reproducibility**. The linear regimes in J.1 and J.2 apply to small contrasts and large angles; corrections of order $\mathcal{O}(z^2)$ and $\mathcal{O}(\alpha^3)$ are to be quantified separately. The construction of $\Lambda_{\rm eff}$ in J.3 assumes stationary phase and spectral separation of operators. Algebraic residuals in J.4 are bounded by Layer I tolerances. The discrete to continuum limit in J.5 assumes consistent schemes and periodic boundaries. All validations use seed 117666 with hash groups G.1–G.7.

*Appendix J.11 Statistical estimators and drift integrals*

This section collects the derivations of the statistical estimators and drift integrals used in Section 6, in particular Eqs. (69)–(77) of the main text.

Appendix J.11.1 Root mean square error (Eq. 69)

Given a set of observed data points $f_n^{\rm obs}$ and model predictions $f_n^{\rm mod}$ for $n = 1, \ldots, N$, the residuals are

$$r_n = f_n^{\rm obs} - f_n^{\rm mod}. \tag{J28}$$

The empirical mean square residual is

$$\mathrm{MSE} = \frac{1}{N}\sum_{n=1}^{N} r_n^2 = \frac{1}{N}\sum_{n=1}^{N}\left(f_n^{\rm obs} - f_n^{\rm mod}\right)^2. \tag{J29}$$

The root mean square error is defined as the positive square root of the mean square residual,

$$\mathrm{RMSE} = \sqrt{\frac{1}{N}\sum_{n=1}^{N}\left(f_n^{\rm obs} - f_n^{\rm mod}\right)^2}, \tag{J30}$$

which coincides with Eq. (69) in the main text. In the Gaussian noise limit, RMSE is an unbiased estimator of the standard deviation of the residual distribution.

Appendix J.11.2 Reduced chi square and goodness of fit (Eq. 70)

For data points $X_i^{\rm obs}$ with model values $X_i^{\rm mod}$ and known standard deviations $\sigma_i$, the (unreduced) chi square statistic is

$$\chi^2 = \sum_{i=1}^{N}\frac{\left(X_i^{\rm obs} - X_i^{\rm mod}\right)^2}{\sigma_i^2}. \tag{J31}$$

If the model has $p$ free parameters, the effective number of degrees of freedom is

$$N_{\rm dof} = N - p. \tag{J32}$$

The reduced chi square is then defined as

$$\chi_\nu^2 = \frac{\chi^2}{N_{\rm dof}} = \frac{1}{N-p}\sum_{i=1}^{N}\frac{\left(X_i^{\rm obs} - X_i^{\rm mod}\right)^2}{\sigma_i^2}, \tag{J33}$$

which reproduces Eq. (70). For correctly estimated uncertainties and a well specified model, one expects $\chi_\nu^2 \simeq 1$.

Appendix J.11.3 Variance decomposition of $H_0$ (Eq. 74)

Let $H_0$ be an estimator that is affected by three statistically independent sources of uncertainty:

- measurement noise with variance $\sigma^2_{\rm meas}$,
- peculiar velocity contributions with variance $\sigma^2_{\rm pv}$,
- cosmic variance with variance $\sigma^2_{\rm cv}$.

Writing

$$\delta H_0 = \delta H_0^{\rm meas} + \delta H_0^{\rm pv} + \delta H_0^{\rm cv}, \tag{J34}$$

and assuming vanishing cross covariances,

$$\left\langle \delta H_0^{\rm meas} \delta H_0^{\rm pv} \right\rangle = \left\langle \delta H_0^{\rm meas} \delta H_0^{\rm cv} \right\rangle = \left\langle \delta H_0^{\rm pv} \delta H_0^{\rm cv} \right\rangle = 0, \tag{J35}$$

one obtains

$$\sigma_{H_0}^2 = \left\langle \delta H_0^2 \right\rangle = \sigma_{\rm meas}^2 + \sigma_{\rm pv}^2 + \sigma_{\rm cv}^2, \tag{J36}$$

which is Eq. (74) in the main text.

Appendix J.11.4 Drift averaging and radial smoothing (Eq. 75)

The local drift $\delta H(\mathbf{x})$ in the linear regime is related to the foreground potential $\Phi_{\rm FG}$ via

$$\delta H(\mathbf{x}) = \frac{1}{3a^2 H_0} \nabla^2 \Phi_{\rm FG}(\mathbf{x}). \tag{J37}$$

To obtain a scale averaged radial drift over a spherical region of radius $R$ and volume $V_R$, one defines

$$\frac{\delta H(R)}{H_0} = \frac{1}{V_R} \int_{V_R} \frac{1}{3a^2 H_0^2} \nabla^2 \Phi_{\rm FG}(\mathbf{x})\, {\rm d}^3 x, \tag{J38}$$

which reproduces the form of Eq. (75). This expression is equivalent to a spherical top hat smoothing of $\delta H / H_0$ in real space.

Appendix J.11.5 Drift variance and potential power spectrum (Eqs. 76–77)

In Fourier space, the potential is written as

$$\Phi_{\rm FG}(\mathbf{x}) = \int \frac{{\rm d}^3 k}{(2\pi)^3}\, \Phi_{\rm FG}(\mathbf{k})\, {\rm e}^{i\mathbf{k}\cdot\mathbf{x}}, \tag{J39}$$

with power spectrum

$$\left\langle \Phi_{\rm FG}(\mathbf{k}) \Phi_{\rm FG}^*(\mathbf{k}') \right\rangle = (2\pi)^3 \delta^{(3)}(\mathbf{k} - \mathbf{k}') P_\Phi(k). \tag{J40}$$

The smoothed drift $\delta H(R)/H_0$ can be written as

$$\frac{\delta H(R)}{H_0} = \int \frac{{\rm d}^3 k}{(2\pi)^3}\, W_R(k)\, \mathcal{K}(k)\, \Phi_{\rm FG}(\mathbf{k}), \tag{J41}$$

where $W_R(k)$ is the Fourier transform of the spherical top hat window of radius $R$, and $\mathcal{K}(k)$ encodes the Laplacian factor and normalization. The variance of the smoothed drift becomes

$$\left\langle \left( \frac{\delta H}{H_0} \right)^2 \right\rangle_R = \int \frac{{\rm d}^3 k}{(2\pi)^3}\, \left| W_R(k) \right|^2 \left| \mathcal{K}(k) \right|^2 P_\Phi(k). \tag{J42}$$

For a narrow window in $k$ around $k \sim 1/R$ and slowly varying $\mathcal{K}(k)$, the integral is dominated by modes near $k \simeq 1/R$, so that

$$\left\langle \left( \frac{\delta H}{H_0} \right)^2 \right\rangle_R \propto R^{-3} P_\Phi(k \simeq 1/R), \tag{J43}$$

which yields the scaling relation quoted in Eq. (76) and the numerical values summarised in Eq. (77).

# Appendix K Glossary of Resonant Terminology

*Appendix K.1 Rationale for a New Lexicon*

The Supra-Omega Resonance Theory (SORT) adopts an operatoric ontology that departs from the particle-based metaphors of both Quantum Field Theory (QFT) and String Theory. Instead of quantized excitations propagating on pre-defined geometries, the fundamental entities of SORT are *idempotent operators* acting within a finite resonance algebra of twenty-two fragments. Each operator defines a stable subspace whose interactions are described by resonant coupling rather than by particle exchange. This shift in ontology demands a corresponding shift in terminology: words derived from geometric or particulate imagery (e.g., "strings," "branes," "bosons") obscure the algebraic nature of the model. The glossary below formalizes the conceptual replacements introduced in SORT and motivates them from both mathematical and physical perspectives.

The replacement scheme is not merely linguistic. It expresses a re-organization of theoretical structure: from geometric propagation on extended manifolds to algebraic resonance within an idempotent operator space. Where String Theory treats consistency through conformal anomaly cancellation, SORT secures internal coherence through light-balance neutrality and structural idempotency. The following sections outline this transition in five conceptual domains: carriers, symmetry, topology, balance, and composition.

*Appendix K.2 From Particles to Resonance Carriers*

In conventional QFT the boson functions as the mediator of forces between matter fields. In String Theory it corresponds to vibrational excitations of one-dimensional strings on a worldsheet. Within SORT, such objects are replaced by resonance carriers—minimal idempotent interactions between fragment operators. Each resonance carrier represents a quantized transfer of structural phase rather than a transport of energy-momentum. Mathematically, it is realized as a local resonance term coupling two idempotent operators $O_i$ and $O_j$ within the total projector $\hat{H} = \sum_i c_i O_i$. The interaction amplitude replaces the field-theoretic propagator.

Because each operator satisfies $O_i^2 = O_i$, resonance carriers do not generate cascades or infinite towers of excitations; they stabilize the algebra by preserving idempotency. This makes the resonance carrier the elementary mediator of coherence in the projection manifold—an analogue to the boson but stripped of geometric assumptions and field-quantization ambiguities.

*Appendix K.3 Light Balance and the Replacement of Central Charge*

String Theory enforces consistency through the central charge $c$, which governs anomaly cancellation and determines the critical dimension of the worldsheet theory. SORT replaces this scalar with the light-balance condition, expressed as the sum of resonance weights $\sum_i c_i = 0$. Here each $c_i$ quantifies the order contribution of a fragment operator to the global structure. The light-balance condition plays the role of an internal conservation law: it ensures that emission and absorption processes in the resonance manifold exactly compensate, yielding zero net amplitude drift. The order contribution thus replaces the central charge as the invariant controlling algebraic consistency.

Where String Theory obtains conformal symmetry through two-dimensional geometry, SORT achieves structural neutrality through the algebraic trace condition $\mathrm{Tr}\,\hat{H} = 0$. This formulation eliminates the need for dimensional fine-tuning or anomaly cancellation in higher-dimensional spaces; balance is enforced directly within the operator algebra.

*Appendix K.4 Structural Equilibrium instead of Anomaly Cancellation*

Anomalies in quantum and string models mark the breakdown of gauge or diffeomorphism invariance. SORT secures consistency through structural equilibrium or resonant balance rather than through compensating fields. The equivalent operation is termed structural re-equilibration or Schwingungsharmonie: a constraint that the total algebra of twenty-two operators remains idempotent and trace-neutral under all admissible compositions. This algebraic constraint replaces the need for Green–Schwarz-type anomaly mechanisms, since all consistency conditions arise internally from the closure relations $[O_i, [O_j, O_k]] + [O_j, [O_k, O_i]] + [O_k, [O_i, O_j]] = 0$ and the residual norm limit $||[O_i, O_j]|| \leq 10^{-12}$. Thus structural equilibrium is the resonant counterpart of anomaly cancellation, ensuring that informational flux through the projection operator is divergence-free at machine precision.

*Appendix K.5 Operatoric Symmetries instead of Supersymmetry*

Supersymmetry introduces a graded algebra linking fermionic and bosonic sectors to secure vacuum energy balance. In SORT, all operators act within a single informational sector; balance is achieved not through fermion–boson duality but through operatoric mirror symmetry or light reflection. Each fragment possesses a dual fragment under complex conjugation and ordering inversion, producing dual resonance pairs that collectively preserve the light-balance condition. This dual-resonant structure replaces supersymmetry while maintaining the essential property of mutual cancellation between conjugate contributions.

Mathematically, the mirror relation $O_i^\dagger = O_j$ with $c_i = -c_j$ defines the pairing rule, guaranteeing that the spectrum of the total operator is symmetric about zero. Hence, where supersymmetry enforces vacuum stability through graded commutation, SORT attains the same through algebraic reflection across its operator spectrum.

*Appendix K.6 From Worldsheet to Resonant Surface*

The geometric foundations of String Theory rely on the worldsheet, the two-dimensional surface swept out by a string in spacetime. SORT discards this geometric dependence and introduces the concept of the resonant surface or vibration skin (Schwingungshaut). It denotes the informational boundary on which the projection kernel $\kappa[\Sigma; \phi_+, \phi_-]$ couples conjugate field configurations. Instead of being an embedding in spacetime, the resonant surface is an operator-defined correlation domain in the projective Hilbert space $H_R$. The kernel normalization $\int_\Sigma |\kappa|^2 \, d\phi_+ \, d\phi_- = 1$ ensures conservation of informational energy along this surface. Thus, what String Theory interprets as geometric area, SORT interprets as algebraic coupling strength; topology arises as a property of correlation rather than geometry.

*Appendix K.7 From D-Branes to Dimensional Membranes*

In String Theory, D-branes serve as boundary objects where strings terminate, defining higher-dimensional submanifolds that mediate interactions between sectors. SORT replaces these geometric constructs with dimensional membranes, algebraic transition layers linking adjacent resonance domains. A dimensional membrane represents the boundary condition between distinct projection levels—analogous to the interface between Layers II and III in the numerical implementation. Mathematically it corresponds to a coupling map between operator subspaces rather than to an extended object in real space. This substitution shifts the explanatory focus from topological embeddings to operatoric connectivity: transitions between states are mediated by projection operators, not by spatial extension.

*Appendix K.8 Resonance Chains instead of Operator Products*

The operator product expansion (OPE) in QFT and String Theory organizes local interactions through series of composite operators. In SORT, this structure is replaced by resonance chains or structural linkages—finite ordered products of idempotent fragments forming the total projector $\hat{H} = \prod_{i=1}^{22} O_i$. Because each factor is idempotent, the chain is stable under iteration and free of divergences. The resonance chain represents a closed algebraic pathway of coherence, through which information flows without loss or amplification. This re-formulation eliminates renormalization issues associated with local products, since the algebra is finite and self-consistent by construction.

*Appendix K.9 Hierarchy within the 22-Fragment Algebra*

All resonant terms and their analogues are organized within a fixed hierarchy of twenty-two operators. Each operator embodies one fragment of the universal resonance manifold, characterized by its order contribution $c_i$ and its domain of action (self-adjoint, unitary, or mixed). Lower fragments describe elementary projection symmetries, while higher fragments represent composite couplings and topological closures. The entire algebra remains idempotent and spectrally neutral, ensuring that global resonance—analogous to a stationary cosmological background—emerges from the balanced superposition of all fragments.

This hierarchy substitutes for the infinite excitation spectra of String Theory: every physical effect arises from the finite combinatorics of fragment interactions rather than from mode expansions on an extended manifold.

*Appendix K.10 Philosophical and Mathematical Motivation*

The terminological transformation reflects a deeper methodological stance. String Theory encodes physical phenomena in geometric form: motion of one-dimensional objects on continuous manifolds. SORT instead interprets structure as emergent from algebraic coherence. Geometry, energy, and time are secondary descriptors of resonant relationships among idempotent operators. This transition—from geometry to algebra, from particles to operators—mirrors the conceptual movement in modern quantum information theory where states are defined relationally rather than ontologically.

Replacing geometric metaphors with resonant ones therefore improves both precision and falsifiability. Quantities such as the light-balance, resonance variance, and projection density can be computed directly from algebraic data and tested against cosmological observables (Hubble drift, CMB anisotropy, effective cosmological constant) without invoking unobservable geometric dimensions.

*Appendix K.11 Conceptual Transparency and Empirical Testability*

By reformulating traditional terminology in operatoric language, SORT achieves a vocabulary that is both mathematically rigorous and physically measurable. Each replacement term corresponds to an explicit algebraic operation or conserved quantity within the model:

- Resonance carrier → measurable coupling amplitude between fragment operators.
- Order contribution → numerical weight determining spectral neutrality.
- Structural equilibrium → closure condition ensuring zero divergence of informational flux.
- Light reflection (dual resonance) → algebraic mirror relation replacing graded supersymmetry.
- Resonant surface → correlation manifold defining non-local projection coupling.

This lexicon links theoretical constructs directly to calculable and reproducible quantities in the simulation pipeline. It allows the theory to be confronted with empirical data—e.g., by deriving observable fields such as $\Phi_{\mathrm{FG}}$ and $\delta H/H_0$—without reliance on untestable geometrical abstractions.

*Appendix K.12 Conclusion*

Appendix K formalizes the linguistic and conceptual framework that distinguishes the Supra-Omega Resonance Theory from traditional string-based or particle-based paradigms. Through the systematic replacement of geometric metaphors by operatoric and resonant constructs, the theory expresses physical law as a network of algebraic coherence relations rather than as dynamics of extended objects. This terminology is not ornamental: it is the logical language of a finite, self-consistent algebra describing cosmological self-coherence. By grounding every concept in idempotency, closure, and light-balance neutrality, the SORT lexicon achieves internal precision while remaining open to empirical falsification through measurable resonance fields in cosmology.